Discontinuous Galerkin Solution of the Boltzmann Equation in Multiple Spatial Dimensions

by

Zhengyi Lian

B.Eng. Mechanical Engineering
National University of Singapore (2006)

Submitted to the School of Engineering
in Partial Fulfillment of the Requirements for the Degree of

Master of Science in Computation for Design and Optimization

at the

MASSACHUSETTS INSTITUTE OF TECHNOLOGY

September 2007

© 2007 Massachusetts Institute of Technology. All rights reserved.

Author .....
School of Engineering
August 16, 2007

Certified by .....
Nicolas G. Hadjiconstantinou
Associate Professor
Thesis Supervisor

Accepted by .....
Jaime Peraire
Professor of Aeronautics and Astronautics
Codirector, Computation for Design and Optimization Program

Discontinuous Galerkin Solution of the Boltzmann Equation in Multiple Spatial Dimensions

by

Zhengyi Lian

Submitted to the School of Engineering
on August 16, 2007, in Partial Fulfillment of the
Requirements for the Degree of
Master of Science in Computation for Design and Optimization

Abstract

This thesis focuses on the numerical solution of a kinetic description of small scale dilute gas flows when the Navier-Stokes description breaks down. In particular, it investigates alternative solution techniques for the Boltzmann equation typically used when the Knudsen number (ratio of molecular mean free path to characteristic length scale of flow) exceeds (approximately) 0.1. Alternative solution methods are required because the prevalent Boltzmann solution technique, Direct Simulation Monte Carlo (DSMC), experiences a sharp rise in computational cost as the deviation from equilibrium decreases, such as in low signal flows. To address this limitation, L. L. Baker and N. G. Hadjiconstantinou recently developed a variance reduction technique [5] in which one only simulates the deviation from equilibrium. This thesis presents the implementation of this variance reduction approach to a Runge-Kutta Discontinuous Galerkin finite element formulation in multiple spatial dimensions. Emphasis is given to alternative algorithms for evaluating the advection operator terms, boundary fluxes and hydrodynamic quantities accurately and efficiently without the use of quadrature schemes. The collision integral is treated as a source term and evaluated using the variance-reduced Monte Carlo technique presented in [10, 9].

For piecewise linear ($p = 1$) and quadratic ($p = 2$) solutions to the Boltzmann equation in 5 spatial dimensions, the developed algorithms are able to compute the advection operator terms by a factor of 2.35 and 2.73 times faster than an algorithm based on quadrature, respectively; with the computation of hydrodynamic quantities, the overall performance improvement is a factor of 8.5 and 10, respectively. Although the collision integral takes up to 90% or more of the total computation cost, these improvements still provide tangible efficiency advantages in steady-flow calculations in which less expensive transient collision-operator calculation routines are used during a substantial part of the flow development.

High order convergence in physical space has been verified by applying the implemented RKDG method on a test problem with a continuous solution. Furthermore, when applied to pressure driven Poiseuille flow through a rectangular channel, the steady state mass flux in the collisionless limit (where exact results exist) agrees within

0.5%, 0.8% and 1.2% of that obtained by Sone and Hasegawa [14] for aspect ratios of 1, 2 and 4 respectively under a spatial resolution of $5^2 \times 10^3$. For $Kn = 0.2, 1$ and 10, our results agree with those obtained by Sone and Hasegawa [14] from solutions of the linearized Boltzmann-Krook-Welander(BKW) equation by comparing them at an "equivalent" Knudsen number of $1.27Kn$ [21]. These results validate the implementation and demonstrate the feasibility of the variance-reduced RKDG method for solving the full Boltzmann equation in multiple spatial dimensions.

To pursue higher accuracy for this pressure driven flow problem, a $p = 1$ scheme was found to be more efficient than a $p = 2$ scheme at a coarser spatial discretization. This can be achieved by using finer spatial discretization and non-uniform spacing to generate more elements near regions of discontinuities or large variations in the molecular distribution function.

Thesis Supervisor: Nicolas G. Hadjiconstantinou
Title: Associate Professor

Acknowledgments

Firstly, I would like to thank my advisor, Nicolas Hadjiconstantinou for his patience, support and encouragement over the course of my graduate studies.

Secondly, I would like to thank Lowell for helping me with the collision integral, code optimization and various aspects of my research.

Next, I would like to thank Ghassan for his help on Latex and various aspects of using Athena.

I would also like to thank my officemates Lowell, Ghassan, Husain, Saeed, Laetitia for making the office such a lively place.

My deepest gratitude goes to my family and girlfriend for their endless love, support and belief in me.

Lastly, I would like to thank the Singapore-MIT Alliance for sponsoring my studies and stay at MIT.

Contents

List of Figures

List of Tables

Chapter 1

Introduction

As the functional parts of micro- and nano-engineered devices become smaller, their mechanical and thermal responses are expected to deviate from well studied continuum behavior. For small scale, dilute gas flows, the validity of the continuum assumption can be quantified by the Knudsen number (Kn), a dimensionless ratio of the molecular mean free path to the characteristic length scale of the flow [1]. At Knudsen numbers $Kn \gtrsim 0.1$, the Navier-Stokes equations of continuum fluid mechanics break down. In such flow regimes, an accurate description of gaseous hydrodynamics requires a kinetic approach such as the Boltzmann equation. The range $0.1 \lesssim Kn \lesssim 10$ corresponds to a flow regime where the full Boltzmann equation must be solved for an accurate description of dilute gas flow. At $Kn \gtrsim 10$, collisions are so infrequent that one can obtain reasonably accurate solutions by neglecting collisions and solving the collisionless Boltzmann equation.

Currently, the prevalent method for solving the Boltzmann equation is Direct Simulation Monte Carlo (DSMC) [2, 3], a stochastic particle simulation technique. Unfortunately, the computational cost of DSMC increases sharply as the deviation from equilibrium decreases, which makes the method computationally inefficient for providing low statistical uncertainty [4] solutions to low speed (or in general, low-signal[1]) flows. To address this limitation, L. L. Baker and N. G. Hadjiconstantinou

[1]Here, low signal flows include flows with low Mach number and/or temperature gradients where the deviation of the distribution function from its initial equilibrium state is small.

recently developed a variance reduction technique [5] in which one only simulates the deviation from equilibrium. The variance reduction technique can be combined with a Runge Kutta Discontinuous Galerkin (RKDG) [6] formulation of the full Boltzmann equation to accurately simulate dilute gas flows at a computational cost that is independent of the deviation from equilibrium.

The discontinuous Galerkin (DG) method is a finite element method capable of providing high order spatial (both physical and velocity space) discretization while allowing for solutions with discontinuities across elements [6, 7]. High order discretization in time for hyperbolic equations can be achieved by combining the DG method with a strong stability preserving Runge-Kutta (RK) time integration scheme [8]. Hence, when implemented with variance reduction, the RKDG [6] method has the potential to efficiently and accurately solve the Boltzmann equation for problems which involve propagating discontinuities while exhibiting arbitrarily small deviations from equilibrium.

The objective of this project is to implement and demonstrate the feasibility of a variance-reduced RKDG solver for the full Boltzmann equation in multiple spatial dimensions. This work follows the development of an efficient variance reduction approach [9, 10] which treats the weak form of the collision integral as a source term at a cost that is comparable to evaluating the advection operator of the Boltzmann equation. This thesis also presents efficient algorithms developed to evaluate, in higher spatial dimensions, the advection operator and hydrodynamic quantities of interest from the discretized molecular distribution function. The effectiveness of these algorithms will be assessed in particular, together with the accuracy and efficiency of the overall method for solving the full Boltzmann equation for small scale, low speed flows in multiple spatial dimensions.

1.1 Overview

The next chapter introduces the kinetic description of gas flow and the Boltzmann equation. A non-dimensional problem formulation is presented and the procedure for

obtaining hydrodynamic fields from the kinetic description is discussed. We also introduce the physical test problem used for validating our results, namely 2-dimensional pressure driven flow through a rectangular channel.

Chapter 3 presents the formulation and implementation details of the RKDG method with variance reduction. Emphasis is given to the alternative algorithms developed to evaluate the advection operator terms, boundary fluxes and hydrodynamic quantities accurately and efficiently without the use of quadrature schemes. A comparison of the computational cost of the new algorithms with standard algorithms based on quadrature is also provided.

Chapter 4 provides validation of our 2-dimensional (in physical space) RKDG implementation using a simple test problem with a continuous solution. The RKDG implementation is validated by comparing the obtained spatial convergence rates with theoretically predicted values. Convergence tests are also performed for disturbances propagating along 1 and 2 spatial dimensions to investigate the effects of dimensionality on the spatial convergence rates.

In chapter 5, the RKDG method is applied, with variance reduction, to the pressure driven flow problem. Convergence in both physical and velocity space is investigated in the collisionless limit using the collisionless Boltzmann equation. Tests are also performed using the full Boltzmann equation to obtain the steady state results for $Kn = 0.2$, 1 and 10.

Finally, conclusions drawn from this thesis and recommendations for future research are given in chapter 6.

Chapter 2

Background

2.1 Kinetic Theory and the Boltzmann Equation

In kinetic theory, the state of a dilute gas can be described [1, 2, 11] by the molecular distribution function $f^* = f^*(\mathbf{x}^*, \mathbf{v}^*, t^*)$, defined such that $f^* d^3\mathbf{x}^* d^3\mathbf{c}^*$ corresponds to the expected number of molecules located in the region $d^3\mathbf{x}^*$ about $\mathbf{x}^*$ with velocities in the range $d^3\mathbf{c}^*$ about $\mathbf{c}^*$ at time t^*. (A * sign indicates that the quantity is dimensional.) The evolution of the distribution function in time is governed by the Boltzmann equation [1, 2, 11]

$$\frac{\partial f^*}{\partial t^*} + \mathbf{c}^* \cdot \frac{\partial f^*}{\partial \mathbf{x}^*} + \mathbf{a}^* \cdot \frac{\partial f^*}{\partial \mathbf{c}^*} = \left[\frac{df^*}{dt^*}\right]_{coll} \tag{2.1}$$

where $\mathbf{a}^* = \mathbf{F}^*/m^*$ is the acceleration due to a body force $\mathbf{F}^*$ acting on a molecule with mass m^*.

The Boltzmann equation is essentially a conservation equation for the distribution function f^* in 6-dimensional phase space (3 dimensional physical space and 3 dimensional velocity space) and remains valid across all flow regimes under general flow conditions[1]. On the left of the equation, the advection operator accounts for changes in f^* (in time) due to changes in molecule positions by virtue of their velocities $\left(\mathbf{c}^* \cdot \frac{\partial f^*}{\partial \mathbf{x}^*}\right)$ and due to changes in molecule velocities by virtue of their accelerations

[1] See [1, 2, 11, 12] for the assumptions inherent in the derivation of the Boltzmann equation

under body forces $\left(\mathbf{a}^* \cdot \frac{\partial f^*}{\partial \mathbf{c}^*}\right)$. The collision integral $\left[\frac{df^*}{dt^*}\right]_{coll}$ accounts for changes in f^* due to impulsive changes in molecule velocities from intermolecular collisions and, for the hard sphere gas studied in this thesis, can be expressed as

$$\left[\frac{df^*}{dt^*}\right]_{coll} = \int\int \left(f_1^{*\prime} f^{*\prime} - f_1^* f^*\right) g^* \sigma^* d^2\Theta \, d^3\mathbf{c}_1^* \tag{2.2}$$

where

$$f^* \equiv f^*\left(\mathbf{x}^*, \mathbf{c}^*, t^*\right) \tag{2.3}$$

$$f_1^* \equiv f^*\left(\mathbf{x}^*, \mathbf{c}_1^*, t^*\right) \tag{2.4}$$

$$f^{*\prime} \equiv f^*\left(\mathbf{x}^*, \mathbf{c}^{*\prime}, t^*\right) \tag{2.5}$$

$$f_1^{*\prime} \equiv f^*\left(\mathbf{x}^*, \mathbf{c}_1^{*\prime}, t^*\right) \tag{2.6}$$

Post collision quantities in equations 2.2, 2.5 and 2.6 are superscripted with a prime. The pre- and post-collision velocities are related through the scattering angle Θ, which extends over the entire unit sphere in equation 2.2 to account for scattering in all possible directions. Integration over $\mathbf{c}_1^*$ extends over the entire space to account for molecules with all possible velocities $\mathbf{c}_1^*$ colliding with the molecule of interest with velocity $\mathbf{c}^*$. Collisions are assumed to be elastic so the relative speed $g^* \equiv \|\mathbf{c}_1^* - \mathbf{c}^*\| = \|\mathbf{c}_1^{*\prime} - \mathbf{c}^{*\prime}\|$. For hard spheres of diameter d^*, the (differential) collision cross-section is given by $\sigma^* = d^{*2}/4$. Details on the interpretation as well as alternative formulations of the collision integral can be obtained from [1, 2, 9, 10].

2.1.1 Non-dimensional Boltzmann Equation

This thesis uses the same set of dimensionless variables defined in [9, 10] and given again here:

$$t = t^*/\bar{t}^* \tag{2.7}$$

$$\mathbf{x} = \mathbf{x}^*/\lambda^* \tag{2.8}$$

$$\mathbf{c} = \mathbf{c}^*/\bar{c}^* \tag{2.9}$$

$$f = \left(\bar{c}^{*3}/\bar{n}^*\right) f^* \tag{2.10}$$

$$\mathbf{a} = (\bar{t}^*/\bar{c}^*)\,\mathbf{a}^* \tag{2.11}$$

$$\sigma = \bar{n}^*\lambda^*\sigma^* \tag{2.12}$$

In other words, the characteristic length scale is chosen as the molecular mean free path λ^* which, in the case of hard sphere gas molecules of diameter d^*, is given by

$$\lambda^* = \frac{1}{\sqrt{2}\pi d^{*2}\bar{n}^*} \tag{2.13}$$

where $\bar{n}^*$ is a reference number density. The characteristic velocity is chosen as the most probable molecular speed

$$\bar{c}^* = \sqrt{\frac{2k^*\bar{T}^*}{m^*}} \tag{2.14}$$

where k^* is the Boltzmann's constant and $\bar{T}^*$ is a reference temperature. The characteristic timescale is chosen to be

$$\bar{t}^* = \frac{\sqrt{2}}{\pi}\frac{\lambda^*}{\bar{c}^*} \tag{2.15}$$

which is also the mean time between collisions for hard sphere gas molecules.

Using the set of dimensionless variables defined from equations 2.7 to 2.12, the

Boltzmann equation can be written as [9, 10]

$$\frac{\partial f}{\partial t} + \frac{\sqrt{\pi}}{2}\mathbf{c} \cdot \frac{\partial f}{\partial \mathbf{x}} + \mathbf{a} \cdot \frac{\partial f}{\partial \mathbf{c}} = \left[\frac{df}{dt}\right]_{coll} \tag{2.16}$$

where the dimensionless form of the collision integral is given by

$$\left[\frac{df}{dt}\right]_{coll} = \frac{\sqrt{\pi}}{2} \int \int \left(f_1' f' - f_1 f\right) g\, \sigma\, d^2\Theta\, d^3\mathbf{c}_1 \tag{2.17}$$

2.1.2 Maxwell Boltzmann Distribution

The Maxwell-Boltzmann distribution is the equilibrium distribution for the Boltzmann equation [1, 11]. Its dimensionless form is given by [1]

$$f^{MB}(\mathbf{c}) \equiv n^{MB} \left(\pi\, T^{MB}\right)^{-3/2} \exp\left(-\frac{\left\|\mathbf{c} - \mathbf{u}^{MB}\right\|^2}{T^{MB}}\right) \tag{2.18}$$

and is completely characterized by the non-dimensional number density $n^{MB} = n^{MB*} / \bar{n}^*$, temperature $T^{MB} = T^{MB*} / \bar{T}^*$, and mean velocity $\mathbf{u}^{MB} = \mathbf{u}^{MB*} / \bar{c}^*$.

2.1.3 Collisionless Boltzmann Equation

As the Knudsen number (Kn) increases, collisions become less frequent and their corresponding effect on the distribution function f decreases. In the limit of $Kn \to \infty$, the contribution from the collision integral in equation 2.16 goes to zero and dilute gas flows can be approximated by the collisionless Boltzmann equation, which is given, in dimensionless form, by

$$\frac{\partial f}{\partial t} + \frac{\sqrt{\pi}}{2}\mathbf{c} \cdot \frac{\partial f}{\partial \mathbf{x}} + \mathbf{a} \cdot \frac{\partial f}{\partial \mathbf{c}} = 0 \tag{2.19}$$

A simplified form of the collisionless Boltzmann equation 2.19 is used in the test problems presented in chapters 4 and 5 to investigate the convergence of the Runge-Kutta Discontinuous Galerkin (RKDG) method in physical and velocity space. In convergence tests, collisions are not desired because they introduce statistical uncertainty

("noise") into the distribution function f, which could saturate the steady-state error and corrupt the spatial convergence rates. In addition, the collisionless Boltzmann equation can be useful in test problems for investigating the accuracy of the RKDG method in capturing propagating discontinuities, since the absence of collisions means that the latter are not smoothed out.

2.1.4 Hydrodynamic Fields

Macroscopic properties of interest, such as the number density n, bulk fluid velocity $\mathbf{u}$, stress tensor $\mathbf{P}$, temperature T and heat flux $\mathbf{q}$, can be obtained from moments of the distribution function f as follows [9]

$$n = \int f d^3\mathbf{c} \tag{2.20}$$

$$u_i = \frac{1}{n}\int c_i f d^3\mathbf{c} \tag{2.21}$$

$$P_{ij} = \int (c_i - u_i)(c_j - u_j) f d^3\mathbf{c} \tag{2.22}$$

$$T = \frac{2}{3n}\int \|\mathbf{c} - \mathbf{u}\| f d^3\mathbf{c} \tag{2.23}$$

$$q_i = \frac{1}{2}\int (c_i - u_i)\|\mathbf{c} - \mathbf{u}\| f d^3\mathbf{c} \tag{2.24}$$

The fluid static pressure p can be computed from the trace of the stress tensor as follows

$$p = \frac{P_{ii}}{3} \tag{2.25}$$

The dimensional values for these properties can be obtained as follows [9]

$$n^* = \bar{n}^* n \tag{2.26}$$

$$\mathbf{u}^* = \bar{c}^* \mathbf{u} \tag{2.27}$$

$$\mathbf{P}^* \text{ (or } p^*) = \bar{n}^* m^* \bar{c}^{*2} \mathbf{P} \text{ (or } p) \tag{2.28}$$

$$T^* = \bar{T}^* T \tag{2.29}$$

$$\mathbf{q}^* = m^* n^* \bar{c}^{*3} \mathbf{q} \tag{2.30}$$

2.2 Pressure Driven Flow Problem

The test problem for this thesis is 2-dimensional flow through a rectangular channel with diffuse walls, driven by a constant pressure gradient $\frac{\partial p}{\partial x_3} = \frac{\Delta p}{\Delta x_3}$ along the channel length (x_3-axis). The computational domain is the channel cross-section of dimensionless length L and width H centered at the origin of the x_1-x_2 plane. The Knudsen number for this problem is defined as

$$Kn = \frac{1}{\min(L,\ H)} = \frac{1}{H} \tag{2.31}$$

since the aspect ratio, defined as

$$AR = \frac{L}{H}, \tag{2.32}$$

is chosen to be larger than 1 for all test cases considered.

We will use the symmetry of the flow about the x_1 and x_2 axes to reduce the computational cost of our calculation. In particular, the computational domain can be reduced to the positive quadrant of the x_1-x_2 plane with dimensionless length $L/2$ and width $H/2$. This gives a factor of 4 reduction in the number of elements required to mesh the spatial domain with the same resolution.

The distribution function f in the domain will be initialized as the equilibrium Maxwell Boltzmann distribution f^{MB} with zero mean velocity. Similarly, the boundary condition for f at the walls $x_1 = L/2$ and $x_2 = H/2$ is f^{MB} with zero mean velocity (the walls are stationary). The boundary conditions at the two symmetry boundaries $x_1 = 0$ and $x_2 = 0$ are imposed as follows,

$$x_1 = 0\text{:}\ \ f(x_1, x_2, c_1, c_2, c_3, t) = f(x_1, x_2, -c_1, c_2, c_3, t) \tag{2.33}$$

$$x_2 = 0\text{:}\ \ f(x_1, x_2, c_1, c_2, c_3, t) = f(x_1, x_2, c_1, -c_2, c_3, t) \tag{2.34}$$

Both implementations capture symmetry in the c_3 component of molecular velocity about the x_1- and x_2-axis. However, they also capture anti-symmetry in c_1 and c_2 about the boundaries $x_1 = 0$ and $x_2 = 0$, respectively. The boundary conditions 2.33

and 2.34 are valid for both stationary walls, as well as walls that are moving towards or away from each other at equal speeds.

The RKDG solutions to this test problem for the collisionless case ($Kn = \infty$) and $0.1 \lesssim Kn \lesssim 10$ will be presented in chapter 5. Results will be compared to those obtained by Sone and Hasegawa [14] to validate the accuracy of our implementation.

Chapter 3

Variance Reduced Discontinuous Galerkin Method

This chapter presents the application of the discontinuous Galerkin (DG) [6] framework with variance reduction to the Boltzmann equation. A strong stability preserving Runge-Kutta time integration scheme [8] is used to provide high order time discretization. This combination, which is known as Runge-Kutta discontinuous Galerkin (RKDG) [6], is very suitable for solving strongly hyperbolic equations, such as the Boltzmann equation. The DG formulation to be presented is similar to that in [9]. Variance reduction is introduced using the technique developed in [5, 9, 10] for evaluating the collision integral term efficiently. However, unlike [9] which focuses on the collision integral implementation, this chapter will focus on an alternative implementation of the advection operator terms to limit the increase in the RKDG computational cost with higher spatial dimensions.

3.1 Formulation

3.1.1 Variance Reduction

As in [5], variance reduction is introduced by separating the distribution function into a deviational and an equilibrium part

$$f = f^d + f^{MB} \tag{3.1}$$

where f^{MB} is an arbitrary equilibrium distribution. For simplicity, f^{MB} will be chosen as a Maxwell-Boltzmann distribution that is independent of space and time, which then allows the Boltzmann equation to be written as

$$\frac{\partial f^d}{\partial t} + \frac{\sqrt{\pi}}{2}\mathbf{c} \cdot \frac{\partial f^d}{\partial \mathbf{x}} + \mathbf{a} \cdot \frac{\partial f^d}{\partial \mathbf{c}} = \left[\frac{df^d}{dt}\right]_{coll} - \mathbf{a} \cdot \frac{\partial f^{MB}}{\partial \mathbf{c}} \tag{3.2}$$

Detailed expressions of the variance-reduced collision integral $\left[\frac{df^d}{dt}\right]_{coll}$ and its weak form can be obtained from [9, 10].

Although the distribution function $f = f^d + f^{MB}$ is defined over a velocity space of infinite span in all dimensions, a truncated velocity space $-4 \leq c_i \leq 4$ ($i = 1$ to 3) is used in the interest of computational efficiency. This is justified in low speed flow problems where the distribution function decays very quickly to zero for large molecular velocities $\mathbf{c}$.

3.1.2 Discontinuous Galerkin(DG) Discretization

The 6 dimensional computational domain $\mathbf{D}$ of physical and velocity space can be discretized into finite elements Ω, which together, make up the discretized domain $\mathbf{D}_h$. The DG formulation aims to find a discretized approximation f_h^d to the deviational distribution f^d within a finite dimensional solution space of functions χ_h^p that are piecewise polynomial up to order p in each dimension within every element Ω but not necessarily continuous across the element boundaries. A more precise definition for

the solution space is given by

$$\chi_h^p = \left[v \in L^2(\mathbf{D}) ;\ v|_\Omega \in \wp^p(\Omega)\ \forall\ \Omega \in \mathbf{D}_h \right] \tag{3.3}$$

The relaxation of continuity across elements allows f_h^d, as well as any member of χ_h^p, to be defined independently within each element as continuous polynomial functions. The projection of f_h^d in any element $\Omega \in \mathbf{D}_h$ can be solved independently by enforcing the variance-reduced Boltzmann equation 3.2 weakly over the element Ω by requiring

$$\int_\Omega v \left(\frac{\partial f_h^d}{\partial t} + \frac{\sqrt{\pi}}{2}\mathbf{c} \cdot \frac{\partial f_h^d}{\partial \mathbf{x}} + \mathbf{a} \cdot \frac{\partial f_h^d}{\partial \mathbf{c}} \right) d^6\Omega = \int_\Omega v \left(\left[\frac{df_h^d}{dt} \right]_{coll} - \mathbf{a} \cdot \frac{\partial f^{MB}}{\partial \mathbf{c}} \right) d^6\Omega \tag{3.4}$$

for all test functions $v \in \chi_h^p$. The test functions v are chosen to be non-zero only across the element Ω, so equation 3.4 also holds when the integrals extend over the entire spatial domain. From this point onwards, to simplify the notation, f^d will be taken to mean the finite element approximation f_h^d.

Within each element Ω, $f^d \equiv f^d(\mathbf{x}, \mathbf{c}, t) \in \chi_h^p$ and $v \equiv v(\mathbf{x}, \mathbf{c})$ can be expanded in terms of a set of basis functions spanning the local polynomial space $\wp^p(\Omega)$ as follows

$$f^d|_\Omega = \sum_{i=1}^{N_s} \hat{f}_{\Omega,i}^d(t)\ \phi_i(\mathbf{x}, \mathbf{c}) \tag{3.5}$$

$$v|_\Omega = \sum_{j=1}^{N_s} \hat{v}_{\Omega,j}\ \phi_j(\mathbf{x}, \mathbf{c}) \tag{3.6}$$

where N_s is the number of basis functions per element and $\hat{f}_{\Omega,i}^d$ is the modal coefficient of the ith basis function for f^d in element Ω. A coordinate transformation $(\mathbf{x}, \mathbf{c}) \rightarrow \left(\vec{\xi}\right)$ can be used to map each element to a reference element where the basis functions $\phi_j(\mathbf{x}, \mathbf{c}) = \phi_j\left(\vec{\xi}\right)$ are defined. The basis functions are also defined to be non-zero only over the element Ω for consistency with the definition of v.

Applying integration by parts, equation 3.4[1] can be expanded into

$$\int_\Omega v\frac{\partial f^d}{\partial t}\,d^6\Omega \;+\int_\Gamma v\,f^d\left(\frac{\sqrt{\pi}}{2}\mathbf{c}\cdot\mathbf{n_x}+\mathbf{a}\cdot\mathbf{n_c}\right)d^5\Gamma\;-$$
$$\int_\Omega f^d\left(\frac{\sqrt{\pi}}{2}\mathbf{c}\cdot\frac{\partial v}{\partial\mathbf{x}}-\mathbf{a}\cdot\frac{\partial v}{\partial\mathbf{c}}\right)d^6\Omega\;=\int_\Omega v\left(\left[\frac{df^d}{dt}\right]_{coll}-\mathbf{a}\cdot\frac{\partial f^{MB}}{\partial\mathbf{c}}\right)d^6\Omega \quad (3.7)$$

where $\mathbf{n_x}$ and $\mathbf{n_c}$ are the outward-normal vectors of the element Ω in physical and velocity space respectively, and $|\mathbf{n_x}|^2+|\mathbf{n_c}|^2=1$; Γ denotes the 5 dimensional surface of the element Ω. In the present work, body forces are negligible so we can set $\mathbf{a}=0$. Next, to apply the pressure gradient $\kappa=\frac{\partial p}{\partial x_3}$ in our test problem, an extra source term [13] is included to the right of equation 3.7, which becomes

$$\overbrace{\int_\Omega v\frac{\partial f^d}{\partial t}\,d^6\Omega}^{\text{mass matrix term}}\;+\;\overbrace{\int_\Gamma vh\,d^5\Gamma}^{\text{surface residual}}\;-\overbrace{\int_\Omega f^d\frac{\sqrt{\pi}}{2}\mathbf{c}\cdot\frac{\partial v}{\partial\mathbf{x}}\,d^6\Omega}^{\text{volume residual}}$$
$$=\;\underbrace{\int_\Omega v\left[\frac{df^d}{dt}\right]_{coll}d^6\Omega}_{\text{collision integral term}}\;+\;\underbrace{\int_\Omega v\,\kappa f^{MB}\,d^6\Omega}_{\text{pressure gradient term}} \quad (3.8)$$

where f^{MB} is the equilibrium distribution and h is the Riemann solution to $f^d\left(\frac{\sqrt{\pi}}{2}\mathbf{c}\cdot\mathbf{n_x}+\mathbf{a}\cdot\mathbf{n_c}\right)=f^d\left(\frac{\sqrt{\pi}}{2}\mathbf{c}\cdot\mathbf{n_x}\right)$ since $\mathbf{a}=0$. As the convective terms in the Boltzmann equation are linear, h is exactly the upwind numerical flux.

Substituting the basis expansions 3.5 and 3.6 into equation 3.8 and requiring the resulting equation to hold for any set of coefficients $\hat{v}_{\Omega,j}$ (i.e. $\forall\; v|_\Omega \in \wp^p(\Omega) \equiv \forall\; v \in \chi_h^p$), we obtain

$$\sum_{i=1}^{N_s}\frac{\partial\hat{f}^d{}_{\Omega,i}}{\partial t}\int_\Omega\phi_j\phi_i\,d^6\Omega\;=\;\overbrace{-\int_\Gamma\phi_j h\,d^5\Gamma\;+\;\frac{\sqrt{\pi}}{2}\sum_{i=1}^{N_s}\hat{f}^d{}_{\Omega,i}\int_\Omega\phi_i\mathbf{c}\cdot\frac{\partial\phi_j}{\partial\mathbf{x}}\,d^6\Omega}^{\text{residual}}$$
$$+\int_\Omega\phi_j\left[\frac{df^d}{dt}\right]_{coll}d^6\Omega\;+\;\int_\Omega\phi_j\,\kappa f^{MB}\,d^6\Omega \quad (3.9)$$

which must hold for all $j=1$ to N_s. Equation 3.9 defines an $N_s\times N_s$ linear system of

[1]Note that f_h^d has been replaced with f^d in 3.4 for simplicity in notation

equations which can be solved independently in each element Ω for $\frac{\partial \hat{f}^d_{\Omega,i}}{\partial t}$. The latter can then be integrated in time using a (strong stability preserving [6]) Runge Kutta method to give the time evolution of $\hat{f}^d{}_{\Omega,i}$, and thus $f^d|_\Omega$.

3.1.3 Boundary Conditions

In the DG formulation, boundary conditions are imposed weakly by specifying the numerical fluxes (the upwind flux in our problem) at the element boundaries. For elements that are adjacent to the channel walls, the diffuse wall boundary condition [11, 15] is imposed at element edges coincident with the wall. Currently, this is the most popular model [15, 16] for capturing the behavior of engineering surfaces of practical interest. This model requires no net mass flux through the wall, which implies that gas molecules cannot penetrate but are reflected back after hitting the wall; particles reflected back from the wall follow a distribution function $n^{wall} f^{wall}(\mathbf{c})$ where

$$f^{wall}(\mathbf{c}) = \left(\pi\, T^{wall}\right)^{-3/2} \exp\left(-\frac{\left\|\mathbf{c}-\mathbf{u}^{wall}\right\|^2}{T^{wall}}\right) \tag{3.10}$$

is a normalized[2] distribution at equilibrium with the wall, $\mathbf{u}^{wall}$ is the wall velocity and T^{wall} is the wall temperature. The variable n^{wall} can be "thought of" as the number density of an infinite expanse of gas in equilibrium with the wall. The mass conservation requirement can be implemented as follows

$$\begin{aligned} \text{(Incoming mass flux)} \quad & \int_{\left(\mathbf{c}-\mathbf{u}^{\text{wall}}\right)\cdot\tilde{n}<0} \left[\left(\mathbf{c}-\mathbf{u}^{\text{wall}}\right)\cdot\tilde{n}\right]\left(f^{MB}+f^d\right) d^3\mathbf{c} = \\ \text{(Outgoing mass flux)} \quad & -\int_{\left(\mathbf{c}-\mathbf{u}^{\text{wall}}\right)\cdot\tilde{n}>0} \left[\left(\mathbf{c}-\mathbf{u}^{\text{wall}}\right)\cdot\tilde{n}\right]\left(n^{\text{wall}} f^{\text{wall}}\right) d^3\mathbf{c} \end{aligned} \tag{3.11}$$

where $\tilde{n}$ is the unit normal to the wall pointing into the gas. Equations 3.11 and 3.10 allow n^{wall} to be determined, which completely determines the distribution $n^{wall} f^{wall}(\mathbf{c})$ of outgoing particles. This formulation is sufficiently robust to be applied to problems with stationary or moving walls in all spatial directions.

[2]Normalized here refers to a distribution with unit number density

3.2 Implementation Details

The following sections provide a description of the implementation details of the variance-reduced RKDG method for solving the Boltzmann equation in 6-dimensional phase space. However, in this thesis, our actual implementation is limited to a 5-dimensional space $(x_1, x_2, c_1, c_2, c_3)$.

3.2.1 Spatial Discretization

In this thesis, a rectangular grid is used to mesh the discretized computational domain $\mathbf{D}_h$ in 6-dimensional phase space. For a general rectangular element Ω bounded between $r_{i,min}$ and $r_{i,max}$ ($i = 1$ to 6), each dimension r_i in phase space can be mapped linearly to a reference element coordinate $-1 \leq \xi_i \leq 1$ using

$$r_i = r_{i_\Omega} + \frac{\xi_i}{2} \Delta r_{i_\Omega} \tag{3.12}$$

where

$$r_i = \begin{cases} x_i & \text{for } i = 1 \text{ to } 3 \\ c_{i-3} & \text{for } i = 4 \text{ to } 6 \end{cases} \tag{3.13}$$

and

$$r_{i_\Omega} = \left(r_{i,min} + r_{i,max}\right)/2 \tag{3.14}$$

$$\Delta r_{i_\Omega} = r_{i,max} - r_{i,min} \tag{3.15}$$

3.2.2 Time Discretization

Time discretization is performed using a third order, strong stability preserving Runge-Kutta (RK3ssp) [8] method. The RK3ssp algorithm to advance one time-step

Δt_k from time t_k to t_{k+1} is accurate up to $O\left(\Delta t_k^3\right)$ and is given by

$$\hat{\mathbf{f}}_\Omega^{d\,(1)} = \hat{\mathbf{f}}_\Omega^d\left(t_k\right) + \Delta t_k\, \tilde{L}\left(\hat{\mathbf{f}}_\Omega^d\left(t_k\right)\right) \tag{3.16}$$

$$\hat{\mathbf{f}}_\Omega^{d\,(2)} = \frac{3}{4}\hat{\mathbf{f}}_\Omega^d\left(t_k\right) + \frac{1}{4}\left[\hat{\mathbf{f}}_\Omega^{d\,(1)} + \Delta t_k\, \tilde{L}\left(\hat{\mathbf{f}}_\Omega^{d\,(1)}\right)\right] \tag{3.17}$$

$$\hat{\mathbf{f}}_\Omega^d\left(t_{k+1}\right) = \frac{1}{3}\hat{\mathbf{f}}_\Omega^d\left(t_k\right) + \frac{2}{3}\left[\hat{\mathbf{f}}_\Omega^{d\,(2)} + \Delta t_k\, \tilde{L}\left(\hat{\mathbf{f}}_\Omega^{d\,(2)}\right)\right] \tag{3.18}$$

where $\hat{\mathbf{f}}_\Omega^d$ is the vector of basis function coefficients for $f^d|_\Omega$ and $\tilde{L}\left(\hat{\mathbf{f}}_\Omega^d\right)$ represents the linear system solution of $\frac{\partial \hat{\mathbf{f}}_\Omega^d}{\partial t}$ in equation 3.9. The maximum stable time-step Δt is determined from the Courant-Friederichs-Levy (CFL) condition

$$\Delta t \leq CFL_{L^2}\frac{2}{\sqrt{\pi}v_{max}}\min\left(\Delta x_i\,,\ i = 1 \text{ to } 3\right) \tag{3.19}$$

where CFL_{L^2} is the CFL number required for L^2 stability of the overall RKDG method. In this thesis, the CFL number is computed as

$$CFL_{L^2} = \frac{1}{2p+1} \tag{3.20}$$

which is a practical but conservative estimate[3] of the numerically determined stability limits for $p \leq 2$ for RK schemes of order 3 [6].

3.2.3 Basis Functions

The basis functions used in this thesis are tensor products of Legendre polynomials, which are defined on the 6-dimensional reference element as

$$\phi_s(\vec{\xi}) = \prod_{k=1}^{6}\psi_{n_k}\left(\xi_k\right) \tag{3.21}$$

where $\psi_{n_k}\left(\xi_k\right)$ $(n_k = 0 \text{ to } p)$ is the Legendre polynomial of order n_k evaluated at coordinate ξ_k in the k^{th} spatial dimension of the reference element. The basis function

[3]For DG discretizations where polynomials of degree p are used together with a $p+1$ stage RK scheme that is accurate up to order $p+1$, equation 3.20 is exact for $0 \leq p \leq 1$ and underestimates the numerically determined stability limits of CFL_{L^2} by less than 5% for $p \geq 2$.

index s, which ranges from 1 to $N_s = (p+1)^6$, is given by

$$s = \sum_{k=1}^{6} n_k \, (p+1)^{6-k} \tag{3.22}$$

A tensor product basis is known to produce a well-conditioned mass matrix for all orders p of the local polynomial space $\wp^p(\Omega)$, thus enhancing stability to the linear system solution for $\frac{\partial \hat{\mathbf{f}^d}_\Omega}{\partial t}$. In addition, the following sections will show that when this basis is used with rectangular elements, a combination of sum factorization and analytical expressions for the inner products and moments of Legendre polynomials can be used to compute the volume residual, surface residual, pressure gradient term, boundary fluxes and hydrodynamic fields accurately without the use of quadrature schemes.

3.2.4 Mass Matrix

The mass matrix is given by the tensor

$$M_{ji} = \int_\Omega \phi_j(\mathbf{r})\phi_i(\mathbf{r}) \, d^6\Omega = J \int_{\hat{\Omega}} \phi_j(\vec{\xi})\phi_i(\vec{\xi}) \, d^6\vec{\xi} \tag{3.23}$$

where $\hat{\Omega}$ is the 6-dimensional reference element, the Jacobian J is given by

$$J = \left| \frac{\partial \mathbf{r}}{\partial \vec{\xi}} \right| = \prod_{i=1}^{6} \left(\frac{\Delta r_{i_\Omega}}{2} \right) \tag{3.24}$$

and Δr_{i_Ω} is the element size as defined in equation 3.15.

By expanding the basis functions ϕ_i and ϕ_j into a tensor product form using equation 3.21, sum factorization can be applied to express M_{ji} as

$$M_{ji} = J \prod_{k=1}^{6} \Psi_{n'_k \, n_k} \tag{3.25}$$

where $0 \leq n_k$ (or n'_k) $\leq p$ and

$$\Psi_{n'_k\, n_k} = \int_{-1}^{1} \psi_{n_k}(\xi_k)\, \psi_{n'_k}(\xi_k)\, d\xi_k = \frac{2}{2n_k+1}\delta_{n_k\, n'_k} \tag{3.26}$$

by applying the orthogonality of Legendre polynomials (see Appendix A). The symbol $\delta_{n_k\, n'_k}$ represents the 2^{nd} order identity tensor. The mass matrix (or basis function) indices j and i can be computed from n'_k and n_k respectively using equation 3.22 for $k = 1$ to 6.

The resultant mass matrix is a $N_s \times N_s$ diagonal matrix and remains constant in all elements Ω. A diagonal mass matrix decouples the linear system 3.9 and reduces the sensitivity of the solution to perturbations in the residual, which is expected to come mainly from the statistical "noise" of evaluating the collision integral term using a particle-based variance reduction approach [9, 10].

3.2.5 Volume Residual

The volume residual for each element Ω is given by the vector

$$VR_j = \frac{\sqrt{\pi}}{2}\sum_{i=1}^{N_s} \hat{f^d}_{\Omega,i} \int_\Omega \phi_i\, \mathbf{c}\cdot\frac{\partial\phi_j}{\partial\mathbf{x}}\, d^6\Omega = \frac{\sqrt{\pi}}{2} J \sum_{m=1}^{3}\left(\frac{2}{\Delta x_{m_\Omega}}\sum_{i=1}^{N_s}\hat{f^d}_{\Omega,i} V_{ji}^m\right) \tag{3.27}$$

where

$$V_{ji}^m = \int_{\hat{\Omega}} \phi_i\, c_m \frac{\partial\phi_j}{\partial\xi_m}\, d^6\vec{\xi}, \tag{3.28}$$

J is the Jacobian defined in equation 3.24, Δx_{m_Ω} is the element size in dimension x_m as defined in equation 3.15 and $\hat{\Omega}$ is the 6-dimensional reference element. The basis indices i and j range from 1 to $N_s = (p+1)^6$, where p is the degree of the local polynomial space in each spatial dimension.

The basis functions ϕ_i and ϕ_j can be expanded into tensor products of Legendre polynomials using equation 3.21. Sum factorization can then be used to express the

integral V_{ji}^{m} as

$$V_{ji}^{m} = \underbrace{\left(\int_{-1}^{1} \psi_{n_m} \frac{d\psi_{n'_m}}{d\xi_m} d\xi_m\right)}_{\Psi'_{n'_m n_m}} \underbrace{\left(\int_{-1}^{1} c_m \psi_{n_{(3+m)}} \psi_{n'_{(3+m)}} d\xi_{(3+m)}\right)}_{[c\Psi]_{n'_{(3+m)} n_{(3+m)}}} \prod_{k=[1,6]\setminus\{m,3+m\}} \Psi_{n'_k n_k} \tag{3.29}$$

where $\Psi_{n'_k n_k}$ is as defined in equation 3.26 and $0 \leq n_k$ (or n'_k) $\leq p$. The basis indices j and i can be computed from n'_k and n_k respectively using equation 3.22 for $k = 1$ to 6.

The derivatives $\frac{d\psi_{n'_m}}{d\xi_m}$ can be expressed in terms of Legendre polynomials and derivatives of order less than n'_m (see Appendix A). Then, by using the orthogonality property in equation 3.26, the second order tensor $\Psi'_{n'_m n_m}$ can be reduced to a sparse, lower triangular, Toeplitz matrix with diagonals alternating between 0 and 2, starting with 0's on the leading diagonal (see Appendix A). This can be expressed concisely as

$$\Psi'_{n'_m n_m} = \begin{cases} 2 & \text{if } n'_m > 0 \text{ and } n_m = n'_m - 1 - 2q \\ 0 & \text{otherwise} \end{cases} \tag{3.30}$$

where q is an integer in the range $0 \leq q \leq \left\lfloor \frac{n'_m - 1}{2} \right\rfloor$.

Next, by expressing the velocity component c_m (in element Ω) in terms of the reference coordinate $\xi_{(3+m)}$ using equation 3.12, $[c\Psi]_{n'_{(3+m)} n_{(3+m)}}$ can be expressed as

$$\begin{aligned} [c\Psi]_{n'_{(3+m)} n_{(3+m)}} &= \int_{-1}^{1} c_m \psi_{n_{(3+m)}} \psi_{n'_{(3+m)}} d\xi_{(3+m)} \\ &= c_{m_\Omega} \Psi_{n'_{(3+m)} n_{(3+m)}} + \frac{\Delta c_{m_\Omega}}{2} \int_{-1}^{1} \xi_{(3+m)} \psi_{n_{(3+m)}} \psi_{n'_{(3+m)}} d\xi_{(3+m)} \end{aligned} \tag{3.31}$$

Using equation 3.26 for $\Psi_{n'_{(3+m)} n_{(3+m)}}$ and a closed form expression for the 1^{st} moment inner product represented by the second term (see Appendix A), $[c\Psi]_{n'_{(3+m)} n_{(3+m)}}$ can

be reduced to a tridiagonal matrix, which can be expressed concisely as

$$[c\Psi]_{d'd} = \begin{cases} c_{m_\Omega} \frac{2}{2d'+1} & \text{if } d = d' \\ \frac{\Delta c_{m_\Omega}}{2} \frac{2d'}{(2d'-1)(2d'+1)} & \text{if } d = d'-1 \\ \frac{\Delta c_{m_\Omega}}{2} \frac{2(d'+1)}{(2d'+1)(2d'+3)} & \text{if } d = d'+1 \\ 0 & \text{otherwise} \end{cases} \tag{3.32}$$

where c_{m_Ω} is the center value of c_m in element Ω and Δc_{m_Ω} is the element size in dimension c_m as defined in equations 3.14 and 3.15 respectively. The tensorial indices d' and d represent the Legendre polynomial orders $n'_{(3+m)}$ and $n_{(3+m)}$ respectively.

If VR_j is computed using sum factorization where V_{ji}^m in equation 3.29 is evaluated using standard Gaussian quadrature, the complexity would be of $O(p+1)^8$ per element. Using the analytical expressions derived for the integrals $\Psi_{n'_k n_k}$, $\Psi'_{n'_m n_m}$ and $[c\Psi]_{n'_{(3+m)} n_{(3+m)}}$, the complexity of evaluating VR_j can be reduced to $O(p+1)^6$.

3.2.6 Surface Residual

The surface residual for each element Ω is given by the vector

$$SR_j = -\frac{\sqrt{\pi}}{2} \sum_s \int_{\Gamma_s} \phi_j \, h_s \, d^5\Gamma_s \tag{3.33}$$

where

$$h_s = \begin{cases} f^{d-}(\mathbf{c} \cdot \mathbf{n_x}) & \text{if } \mathbf{c} \cdot \mathbf{n_x} \geq 0 \\ f^{d+}(\mathbf{c} \cdot \mathbf{n_x}) & \text{if } \mathbf{c} \cdot \mathbf{n_x} < 0 \end{cases} \tag{3.34}$$

represents the upwind flux $f^d(\mathbf{c} \cdot \mathbf{n_x})$ through the 5-dimensional surface Γ_s. Each surface Γ_s lies between two adjacent elements Ω^+ and Ω^- and is characterized by a 6-dimensional surface normal $\mathbf{n} = [\mathbf{n_x}\ \mathbf{n_c}]$ which points in the direction of Ω^+. In this thesis, body force accelerations are neglected, which means that there is zero flux through the surfaces with normals "pointing in" (or having a non-zero component) in the velocity space dimensions. Hence, Γ_s only corresponds to the 5-dimensional surfaces with normals $\mathbf{n} = [\mathbf{n_x}\ \mathbf{0}]$ pointing in the physical space dimensions. The superscript $+$ or $-$ denotes if the value of f^d at the surface Γ_s is evaluated within the

adjacent element Ω^+ or Ω^- respectively.

In the case of rectangular elements, $\mathbf{n_x}$ corresponds to standard unit vectors pointing along the principal axes in physical space. Hence,

$$\mathbf{c} \cdot \mathbf{n_x} = \begin{cases} c_m & \text{if} \quad \mathbf{n_x} = \mathbf{e_m} \\ - \; c_m & \text{if} \quad \mathbf{n_x} = -\mathbf{e_m} \end{cases} \tag{3.35}$$

where $\mathbf{e_m}$ is the standard unit vector in physical space with a '1' in component m (m = 1, 2 or 3). Furthermore, the surface Γ_s can be treated as a 5-dimensional rectangle Γ_m^+ at $x_m = x_{m,max}$ or Γ_m^- at $x_m = x_{m,min}$. This can be mapped to a 5 dimensional reference surface $\hat{\Gamma}_m^+$ at $\xi_m = 1$ or $\hat{\Gamma}_m^-$ at $\xi_m = -1$.

In the remainder of this section, the algorithm to evaluate the surface integral $I_s = \int_{\Gamma_s} \phi_j \, h_s \, d^5\Gamma_s$ will be described for the case of $\mathbf{n_x} = e_m$ at the surface $\Gamma_s = \Gamma_m^+$ for simplicity in notation. Using the above simplification for rectangular elements and the tensor product basis expansion for ϕ_j, I_s can be expressed as

$$\begin{aligned} I_s &= \int_{\Gamma_m^+} \phi_j f^{d\pm} \, c_m \, d^5\Gamma_m^+ \\ &= J_m \left[\psi_{n'_m} (\xi_m) \big|_{(\xi_m = 1)} \right] \int_{\hat{\Gamma}_m^+} \left[\prod_{k=[1,6]\setminus\{m\}} \psi_{n'_k} (\xi_k) \right] f^{d\pm} \, c_m \, d^5\hat{\Gamma}_m^+ \end{aligned} \tag{3.36}$$

where $f^{d\pm}$ denotes the appropriate upwind value for f^d, $1 \leq j \leq N_s = (p+1)^6$ and $0 \leq n'_k \leq p$ (k = 1 to 6). The surface Jacobian J_m is given by

$$J_m = \prod_{k=[1,6]\setminus\{m\}} \left(\frac{\Delta r_{k_{\Gamma_s}}}{2} \right) \tag{3.37}$$

where $\Delta r_{k_{\Gamma_s}}$ and r_k are as defined in equations 3.15 and 3.13 respectively. For surfaces Γ_s that coincide with the domain boundaries, f^d is evaluated based on the boundary conditions described in section 3.1.3 and I_s is then evaluated using standard Gaussian quadrature. For surfaces that coincide with internal element boundaries, f^d can be expanded in terms of its tensor product basis functions using equations 3.5 and 3.21,

which allows I_s to be reduced, using sum factorization, to

$$I_s = J_m \sum_{i=1}^{N_s} \hat{f}^d_{\Omega^\pm,i} \left[\psi_{n_m} \psi_{n'_m} \big|_{(\xi_m=1)} \right] [c\Psi]_{n'_{(3+m)} n_{(3+m)}} \prod_{k=[1,6]\setminus\{m,3+m\}} \Psi_{n'_k n_k} \tag{3.38}$$

where $\hat{f}^d_{\Omega^\pm,i}$ denotes the value for $\hat{f}^d_{\Omega,i}$ evaluated in the appropriate element Ω^+ or Ω^- based on upwinding. The tensors $[c\Psi]_{n'_{(3+m)} n_{(3+m)}}$ and $\Psi_{n'_k n_k}$ are as defined in equations 3.31 and 3.26 respectively. The basis indices j and i can be computed from n'_k and n_k respectively using equation 3.22 for $k = 1$ to 6. In the case of $\Gamma_s = \Gamma^-_m$, the Legendre polynomials ψ_{n_m} and $\psi_{n'_m}$ are evaluated at $\xi_m = -1$ instead of $\xi_m = 1$. For $\mathbf{n_x} = -e_m$, a negative sign should be added to c_m in equation 3.36 and to $[c\Psi]_{n'_{(3+m)} n_{(3+m)}}$ in equation 3.38.

The complexity of evaluating SR_j would scale with $O(p+1)^8$ per element if Gaussian quadrature is used with sum factorization. With the analytical expressions derived for $\Psi_{n'_k n_k}$ and $[c\Psi]_{n'_{(3+m)} n_{(3+m)}}$, the complexity can be reduced to $O(p+1)^6$.

3.2.7 Pressure Gradient Term

The pressure gradient term for each element Ω is given by the vector

$$PR_j = J\,\kappa \int_{\hat{\Omega}} \phi_j\, f^{MB}\, d^6\hat{\Omega} \tag{3.39}$$

where J is the Jacobian as defined in equation 3.24, $\kappa = \frac{\partial p}{\partial x_3}$ is the applied pressure gradient, f^{MB} is the equilibrium distribution and $\hat{\Omega}$ is the 6-dimensional reference element.

By expanding ϕ_j in a tensor product form using equation 3.21 and using the definition of f^{MB} in equation 2.18, sum factorization can be used to express PR_j as

$$PR_j = J\,\kappa\, n^{MB} \left(\pi T^{MB}\right)^{-3/2} \prod_{m=1}^{3} \left(\Psi_{n_m} \left[\Psi \exp(c^2) \right]_{n_{(3+m)}} \right) \tag{3.40}$$

where

$$\Psi_{n_m} = \int_{-1}^{1} \psi_{n_m} d\xi_m = \begin{cases} 2 & \text{for } n_m = 0 \\ 0 & \text{otherwise} \end{cases} \tag{3.41}$$

using the orthogonality of Legendre polynomials and

$$\left[\Psi \exp(c^2)\right]_{n_{(3+m)}} = \int_{-1}^{1} \psi_{n_{(3+m)}} \exp\left(\frac{\left(c_m - u_m^{MB}\right)^2}{T^{MB}}\right) d\xi_{(3+m)} \tag{3.42}$$

, which can be evaluated using standard Gaussian quadrature.

The vector(or basis) index j can be computed from n_k using equation 3.22 for $k = 1$ to 6. The Legendre polynomial order n_k ranges from 0 to p , where p is the degree of the local polynomial space in each dimension. The fact that Ψ_{n_m} is non-zero only for $n_m = 0$ implies that out of the $(p+1)^6$ components in PR_j, only the first $(p+1)^3$ components are non-zero and need to be computed. Furthermore, the tensors $[\Psi \exp(c^2)]_{n_{(3+m)}}$ $(m = 1$ to $3)$ can be pre-computed at a complexity of $O(p+1)^2$ using Gaussian quadrature. Hence, the overall complexity of computing PR_j for each element only scales with $O(p+1)^3$.

3.2.8 Boundary Flux

The diffuse wall boundary condition in equation 3.11 can be expressed as

$$F^d + F^{MB} = n^{\text{wall}} F^{\text{wall}} \tag{3.43}$$

which requires the evaluation of the following boundary fluxes.

$$F^d = \int_{\left(\mathbf{c}-\mathbf{u}^{\text{wall}}\right)\cdot\tilde{n}<0} \left[\left(\mathbf{c}-\mathbf{u}^{\text{wall}}\right)\cdot\tilde{n}\right] f^d d^3\mathbf{c} \tag{3.44}$$

$$F^{MB} = \int_{\left(\mathbf{c}-\mathbf{u}^{\text{wall}}\right)\cdot\tilde{n}<0} \left[\left(\mathbf{c}-\mathbf{u}^{\text{wall}}\right)\cdot\tilde{n}\right] f^{MB} d^3\mathbf{c} \tag{3.45}$$

$$F^{\text{wall}} = \int_{\left(\mathbf{c}-\mathbf{u}^{\text{wall}}\right)\cdot\tilde{n}>0} \left[\left(\mathbf{c}-\mathbf{u}^{\text{wall}}\right)\cdot\tilde{n}\right] f^{\text{wall}} d^3\mathbf{c} \tag{3.46}$$

where the symbols are as defined in section 3.1.3. In the case of rectangular elements, the normal components of the gas molecule and wall velocity to the wall $x_m = constant$ ($m = 1, 2$ or 3) can be expressed respectively as

$$\mathbf{c} \cdot \tilde{n} = \begin{cases} c_m & \text{if } x_m = x_{m,min} \\ -c_m & \text{if } x_m = x_{m,max} \end{cases} \tag{3.47}$$

and

$$\mathbf{u}^{\text{wall}} \cdot \tilde{n} = \begin{cases} u_m^w & \text{if } x_m = x_{m,min} \\ -u_m^w & \text{if } x_m = x_{m,max} \end{cases} \tag{3.48}$$

This allows the boundary fluxes to be written, for the wall $x_m = x_{m,max}$, as

$$F^d = \int_{c_m > u_m^w} (c_m - u_m^w)\, f^d d^3\mathbf{c} \tag{3.49}$$

$$F^{MB} = \int_{c_m > u_m^w} (c_m - u_m^w)\, f^{MB} d^3\mathbf{c} \tag{3.50}$$

$$F^{\text{wall}} = \int_{c_m < u_m^w} (c_m - u_m^w)\, f^{\text{wall}} d^3\mathbf{c} \tag{3.51}$$

If the wall $x_m = x_{m,min}$ is considered, the condition on the integration limits for F^d and F^{MB} are changed to $c_m < u_m^w$ while that for F^{wall} is changed to $c_m > u_m^w$.

Using equations 3.5 and 3.21, f^d can be expanded in its tensor product basis, which allows F^d to be written as

$$F^d = \sum_{\forall\, \Omega_v} \sum_{i=1}^{N_s} \hat{f}^d_{\Omega_v,i} \left(\prod_{k=1}^{3} \psi_{n_k} \right) \int_{\Omega_v} \left((c_m - u_m^w)\, \psi_{n_{(3+m)}} \right) \left(\prod_{k=[4,6]\setminus\{3+m\}} \psi_{n_k} \right) d^3\Omega_v \tag{3.52}$$

where Ω_v refers to a 3-dimensional element in velocity space which satisfy the appropriate condition imposed on the integration limits for F^d. The index i can be computed from n_k using equation 3.22 for $k = 1$ to 6. At this point, it would be convenient to express $\sum_{i=1}^{N_s} = \sum_{n_1=0}^{p} \sum_{n_2=0}^{p} \sum_{n_3=0}^{p} \sum_{n_4=0}^{p} \sum_{n_5=0}^{p} \sum_{n_6=0}^{p}$ and the vector $\hat{f}^d_{\Omega_v,i}$ as a 7-dimensional tensor $\hat{f}^d_{\Omega_v,n_1,n_2,n_3,n_4,n_5,n_6}$. Next, by expressing the integrals over a 3-dimensional cubic reference element $\hat{\Omega}_v$ and using sum factorization, F^d, for

the case of $m = 1$, can be written as

$$F^d = J_v \sum_{\forall \Omega_v} \sum_{n_1,n_2,n_3=0}^{p} \psi_{n_1}\psi_{n_2}\psi_{n_3} \sum_{n_4=0}^{p} \left[(c-u^w)\Psi\right]_{n_4} \sum_{n_5=0}^{p} \Psi_{n_5} \sum_{n_6=0}^{p} \Psi_{n_6} \hat{f}^d_{\Omega_v,n_1,n_2,n_3,n_4,n_5,n_6} \tag{3.53}$$

where Ψ_{n_k} is as defined in equation 3.41 for $k = 1$ to 6 and the symbol $\sum_{n_1,n_2,n_3=0}^{p} \equiv \sum_{n_1=0}^{p}\sum_{n_2=0}^{p}\sum_{n_3=0}^{p}$. The term

$$\left[(c-u^w)\Psi\right]_{n_{(3+m)}} = \int_{-1}^{1} (c_m - u^w_m)\,\psi_{n_{(3+m)}} d\xi_{(3+m)} = \begin{cases} 2\left(c_{m_{\Omega_v}} - u^w_m\right) & \text{if } n_{(3+m)} = 0 \\ \frac{\Delta c_{m_{\Omega_v}}}{3} & \text{if } n_{(3+m)} = 1 \\ 0 & \text{otherwise} \end{cases} \tag{3.54}$$

by expressing c_m (in element Ω_v) in terms of the reference coordinate $\xi_{(3+m)}$ using equation 3.12 and using analytical expressions for the 0^{th} and 1^{st} moment of Legendre polynomials (see Appendix A). The velocity space Jacobian J_v for an element Ω is given by

$$J_v = \prod_{m=1}^{3} \frac{\Delta c_{m_\Omega}}{2} \tag{3.55}$$

Using the derived expressions for Ψ_{n_k} and $\left[(c-u^w)\Psi\right]_{n_{(3+m)}}$ in equations 3.41 and 3.54, equation 3.53 can be simplified to

$$F^d = 4J_v \sum_{\forall \Omega_v} \sum_{n_1,n_2,n_3=0}^{p} \psi_{n_1}\psi_{n_2}\psi_{n_3} \left(2\left(c_{m_{\Omega_v}} - u^w_m\right)\hat{f}^d_{\Omega_v,n_1,n_2,n_3,0,0,0} + \frac{\Delta c_{m_{\Omega_v}}}{3}\hat{f}^d_{\Omega_v,n_1,n_2,n_3,1,0,0}\right) \tag{3.56}$$

where $m = 1$. For $m = 2$ or 3, the expression for F^d in equation 3.56 still holds by replacing the last 3 tensorial indices of the second $\hat{f}^d$ term from $(1,0,0)$ to $(0,1,0)$ or $(0,0,1)$ respectively.

The boundary flux F^{MB} can be expressed analytically as (see Appendix B)

$$F^{MB} = n^{MB}\left[\mp\frac{1}{2}\sqrt{\frac{T^{MB}}{\pi}}\exp\left(-\frac{u^2_{rel}}{T^{MB}}\right) - \frac{u_{rel}}{2}\left(1 + \text{sgn}(\mathbf{u}^{\text{wall}}\cdot\tilde{n})\,\text{erf}\left(\frac{u_{rel}}{\sqrt{T^{MB}}}\right)\right)\right] \tag{3.57}$$

where

$$\text{erf}\left(\frac{u_{rel}}{\sqrt{T^{MB}}}\right) = \frac{2}{\sqrt{\pi}} \int_0^{\frac{u_{rel}}{\sqrt{T^{MB}}}} \exp\left(-y^2\right) dy \tag{3.58}$$

is the error function evaluated at $\frac{u_{rel}}{\sqrt{T^{MB}}}$, $u_{rel} = u_m^w - u_m^{MB}$ and u_m^{MB} is the mean velocity corresponding to the equilibrium distribution f^{MB}. The dimensionless number density and temperature characterizing the chosen equilibrium distribution f^{MB} are n^{MB} and T^{MB} respectively, which are both set to 1 in this thesis. The signs $\mp$ in F^{MB} correspond, respectively, to boundary fluxes evaluated at the walls $x_m = x_{m,min}$ or $x_m = x_{m,max}$ ($m = 1, 2$ or 3). The expression "$\text{sgn}(\mathbf{u}^{\text{wall}} \cdot \tilde{n})$" takes on a value of $+1$ or -1 when the walls are moving towards or apart from each other respectively. In this thesis, $u_{rel} = 0$ as both u_m^w and $\mathbf{u}^{MB}$ are chosen to be zero. Hence, $\text{erf}\left(\frac{u_{rel}}{\sqrt{T^{MB}}}\right) = 0$, which allows F^{MB} to be evaluated analytically without reference to tabulated results of the error function.

The boundary flux F^{wall} can also be evaluated analytically as (see Appendix B)

$$F^{\text{wall}} = \pm\frac{1}{2}\sqrt{\frac{T^{\text{wall}}}{\pi}} \tag{3.59}$$

where T^{wall} represents the dimensionless wall temperature and is set to 1 for all the walls in this thesis. The signs $\pm$ in F^{wall}, correspond, respectively, to boundary fluxes evaluated at the walls $x_m = x_{m,min}$ or $x_m = x_{m,max}$ ($m = 1, 2$ or 3).

3.2.9 Moments of the Distribution Function

The hydrodynamic quantities are computed from moments of the distribution function $f = f^{MB} + f^d$ in velocity space. This section focuses on efficient algorithms developed to evaluate the 0^{th}, 1^{st} and 2^{nd} moments of f^{MB} and f^d in velocity space.

The moments of the equilibrium distribution f^{MB} defined in equation 2.18 are

given by (see Appendix B for derivation details)

$$F^{0,MB} = \int f^{MB} d^3\mathbf{c} = n^{MB} \tag{3.60}$$

$$F_m^{1,MB} = \int c_m f^{MB} d^3\mathbf{c} = n^{MB}\, u_m^{MB} \tag{3.61}$$

$$F_m^{2,MB} = \int c_m^2 f^{MB} d^3\mathbf{c} = n^{MB} \left(\left(u_m^{MB}\right)^2 + \frac{T^{MB}}{2} \right) \tag{3.62}$$

$$F_{mj}^{\text{cross},MB} = \int c_m c_j f^{MB} d^3\mathbf{c} = n^{MB}\, u_m^{MB}\, u_j^{MB} \tag{3.63}$$

The 0^{th} moment of the deviational distribution f^d can be evaluated as follows

$$F^0 = \int f^d d^3\mathbf{c} \tag{3.64}$$

$$= \sum_{\forall\, \Omega_c} \sum_{i=1}^{N_s} \hat{f}_{\Omega,i}^d \int_{\Omega_c} \phi_i d^3\mathbf{c}$$

$$= J_v \sum_{\forall\, \Omega_c} \sum_{n_k=0, k=[1,6]}^{p} \hat{f}_{\Omega_v, n_1, n_2, n_3, n_4, n_5, n_6}^d \left(\prod_{k=1}^{3} \psi_{n_k} \right) \left(\prod_{k=4}^{6} \Psi_{n_k} \right) \tag{3.65}$$

The symbol $\sum_{n_k=0,k=[1,6]}^{p} \equiv \sum_{n_1=0}^{p} \sum_{n_2=0}^{p} \sum_{n_3=0}^{p} \sum_{n_4=0}^{p} \sum_{n_5=0}^{p} \sum_{n_6=0}^{p}$. J_v is the velocity space Jacobian defined in equation 3.55 and Ω_c refers to a 3-dimensional velocity space element at the point (x_1, x_2, x_3) in physical space where F^0 is evaluated. The 0^{th} moment Ψ_{n_k} of a Legendre polynomial ψ_{n_k} is as defined in equation 3.41 based on Legendre orthogonality, which allows equation 3.65 to be simplified to

$$\int f^d d^3\mathbf{c} = \sum_{\forall\, \Omega_c} \sum_{n_1, n_2, n_3=0}^{p} \left(\prod_{k=1}^{3} \psi_{n_k} \right) \hat{f}_{\Omega_v, n_1, n_2, n_3, 0, 0, 0}^d \tag{3.66}$$

The Legendre polynomials ψ_{n_k} are evaluated at the reference element coordinate ξ_k corresponding to the physical space coordinate x_k ($k = 1$ to 3) where the moment F^0 is evaluated. This applies to the rest of the moments defined below as well.

The 1^{st} moment of f^d is given by

$$F_m^1 = \int c_m f^d d^3\mathbf{c} = \sum_{\forall\,\Omega_c} \sum_{i=1}^{N_s} \hat{f}^d_{\Omega,i} \int_{\Omega_c} c_m \phi_i d^3\mathbf{c}$$

For the case of m=1, F_m^1 can be expressed as

$$F_m^1 = J_v \sum_{\forall\,\Omega_c} \sum_{n_k=0,k=[1,6]}^{p} \hat{f}^d_{\Omega_v,n_1,n_2,n_3,n_4,n_5,n_6} \left(\prod_{k=1}^{3} \psi_{n_k}\right) [c\Psi]_{n_4} \Psi_{n_5} \Psi_{n_6} \tag{3.67}$$

where

$$[c\Psi]_{n_{(3+m)}} = \int_{-1}^{1} c_m \psi_{n_{(3+m)}} d\xi_{(3+m)} = \begin{cases} 2c_{m_{\Omega_c}} & \text{if } n_{(3+m)} = 0 \\ \frac{\Delta c_{m_{\Omega_c}}}{3} & \text{if } n_{(3+m)} = 1 \\ 0 & \text{otherwise} \end{cases} \tag{3.68}$$

by expanding c_m using equation 3.12 and applying the analytical expressions for the 0^{th} and 1^{st} moments of Legendre polynomials (see Appendix A). Using the derived expressions for Ψ_{n_k} and $[c\Psi]_{n_{(3+m)}}$ in equations 3.41 and 3.68, equation 3.67 can be simplified to

$$F_m^1 = 4J_v \sum_{\forall\,\Omega_c} \sum_{n_1,n_2,n_3=0}^{p} \left(\prod_{k=1}^{3} \psi_{n_k}\right) \left(2c_{m_{\Omega_c}} \hat{f}^d_{\Omega_v,n_1,n_2,n_3,0,0,0} + \frac{\Delta c_{m_{\Omega_c}}}{3} \hat{f}^d_{\Omega_v,n_1,n_2,n_3,1,0,0}\right) \tag{3.69}$$

where $m = 1$. For $m = 2$ or 3, equation 3.69 should be modified by replacing the last 3 tensorial indices of the second $\hat{f}^d$ term from $(1,0,0)$ to $(0,1,0)$ or $(0,0,1)$ respectively.

The 2^{nd} principal moment of f^d is given by

$$F_m^2 = \int c_m^2 f^d d^3\mathbf{c} = \sum_{\forall\,\Omega_c} \sum_{i=1}^{N_s} \hat{f}^d_{\Omega,i} \int_{\Omega_c} c_m^2 \phi_i d^3\mathbf{c}$$

For the case of m=1, F_m^2 can be expressed as

$$F_m^2 = J_v \sum_{\forall\,\Omega_c} \sum_{n_k=0,k=[1,6]}^{p} \hat{f}^d_{\Omega_v,n_1,n_2,n_3,n_4,n_5,n_6} \left(\prod_{k=1}^{3} \psi_{n_k}\right) \left[c^2\Psi\right]_{n_4} \Psi_{n_5} \Psi_{n_6} \tag{3.70}$$

where

$$\left[c^2\Psi\right]_{n_{(3+m)}} = \int_{-1}^{1} c_m^2 \psi_{n_{(3+m)}} d\xi_{(3+m)} = \begin{cases} 2c_{m_{\Omega_c}} + \frac{\Delta c_{m_{\Omega_c}}}{6} & \text{if } n_{(3+m)} = 0 \\ \frac{2c_{m_{\Omega_c}} \Delta c_{m_{\Omega_c}}}{3} & \text{if } n_{(3+m)} = 1 \\ \frac{\Delta c_{m_{\Omega_c}}^2}{15} & \text{if } n_{(3+m)} = 2 \\ 0 & \text{otherwise} \end{cases} \tag{3.71}$$

by expanding c_m using equation 3.12 and applying the analytical expressions for the 0^{th}, 1^{st} and 2^{nd} moments of Legendre polynomials (see Appendix A). Using the derived expressions for Ψ_{n_k} and $\left[c^2\Psi\right]_{n_{(3+m)}}$ in equations 3.41 and 3.71, equation 3.70 can be simplified to

$$F_m^2 = 4J_v \sum_{\forall\,\Omega_c} \sum_{n_1,n_2,n_3=0}^{p} \left(\prod_{k=1}^{3} \psi_{n_k}\right) \begin{pmatrix} \left(2c_{m_{\Omega_c}} + \frac{\Delta c_{m_{\Omega_c}}}{6}\right) \hat{f}^d_{\Omega_v,n_1,n_2,n_3,0,0,0} \\ + \frac{2c_{m_{\Omega_c}} \Delta c_{m_{\Omega_c}}}{3} \hat{f}^d_{\Omega_v,n_1,n_2,n_3,1,0,0} \\ + \frac{\Delta c_{m_{\Omega_c}}^2}{15} \hat{f}^d_{\Omega_v,n_1,n_2,n_3,2,0,0} \end{pmatrix} \tag{3.72}$$

where $m = 1$. For $m = 2$, equation 3.72 should be modified by replacing the last 3 tensorial indices of the second and third $\hat{f}^d$ term to $(0, 1, 0)$ and $(0, 2, 0)$ respectively. For $m = 3$, the corresponding tensorial indices should be changed to $(0, 0, 1)$ and $(0, 0, 2)$ respectively.

The 2^{nd} cross moment of f^d is given by

$$F_{mj}^{\text{cross}} = \int c_m c_j f^d d^3\mathbf{c} = \sum_{\forall\,\Omega_c} \sum_{i=1}^{N_s} \hat{f}^d_{\Omega,i} \int_{\Omega_c} c_m c_j \phi_i d^3\mathbf{c}$$

For the case of m=1 and j=2, F_{mj}^{cross} can be expressed as

$$F_{mj}^{\text{cross}} = J_v \sum_{\forall\,\Omega_c} \sum_{n_k=0,k=[1,6]}^{p} \hat{f}^d_{\Omega_v,n_1,n_2,n_3,n_4,n_5,n_6} \left(\prod_{k=1}^{3} \psi_{n_k}\right) \left[c\Psi\right]_{n_4} \left[c\Psi\right]_{n_5} \Psi_{n_6} \tag{3.73}$$

Using the derived expressions for Ψ_{n_k} and $\left[c\Psi\right]_{n_{(3+m)}}$ in equations 3.41 and 3.68,

equation 3.73 can be simplified to

$$F_{mj}^{\text{cross}} = 2J_v \sum_{\forall\,\Omega_c} \sum_{n_1,n_2,n_3=0}^{p} \left(\prod_{k=1}^{3} \psi_{n_k} \right) \left(\begin{array}{l} 4c_{m_{\Omega_c}} c_{j_{\Omega_c}} \hat{f}^d_{\Omega_v,n_1,n_2,n_3,0,0,0} \\ + \frac{2c_{m_{\Omega_c}} \Delta c_{j_{\Omega_c}}}{3} \hat{f}^d_{\Omega_v,n_1,n_2,n_3,0,1,0} \\ + \frac{2\Delta c_{m_{\Omega_c}} c_{j_{\Omega_c}}}{3} \hat{f}^d_{\Omega_v,n_1,n_2,n_3,1,0,0} \\ + \frac{\Delta c_{m_{\Omega_c}} \Delta c_{j_{\Omega_c}}}{9} \hat{f}^d_{\Omega_v,n_1,n_2,n_3,1,1,0} \end{array} \right) \tag{3.74}$$

where $m = 1$ and $j = 2$. For other combinations of m and j, equation 3.74 can be modified by changing the tensorial indices of the last 3 $\hat{f}^d$ terms as follows: the tensorial index $n_{(3+k)}$ of the $\hat{f}^d$ term is a 1 only if the $\hat{f}^d$ term has a coefficient that contains $\Delta c_{k_{\Omega_c}}$ where $k = 1, 2$ or 3. Otherwise, $n_{(3+k)} = 0$.

From the computed moments above, the following hydrodynamic quantities can be evaluated at any point (x_1, x_2, x_3) in physical space follows:

$$n = F^0 + F^{0,MB} \tag{3.75}$$

$$u_m = \frac{F_m^1 + F_m^{1,MB}}{n} \tag{3.76}$$

$$P_{m,m} = \int (c_m - u_m)^2 f d^3\mathbf{c} = F_m^{\text{cross}} + F_m^{\text{cross},MB} - n u_m^2 \tag{3.77}$$

$$P_{m,j} = \int (c_m - u_m)(c_j - u_j) f d^3\mathbf{c} = F_{mj}^{\text{cross}} + F_{mj}^{\text{cross},MB} - n u_m u_j \tag{3.78}$$

The proposed algorithms reduced the complexity of evaluating the moments of the distribution function to $O(p+1)^3$ per element in velocity space, which is a significant improvement when compared to $O(p+1)^8$ per element if the moments were evaluated using sum factorization and Gaussian quadrature.

3.3 Performance Evaluation

The variance-reduced RKDG method described in this chapter has been implemented for the Boltzmann equation in 2 physical space dimensions and 3 velocity space dimensions. This section will compare the performance of the proposed algorithms in computing the advection operator terms and hydrodynamic quantities with an

algorithm that utilizes Gaussian quadrature with sum factorization.

The collisionless Boltzmann equation 2.19 is used to compare the computational cost for the volume and surface residual, which come directly from the discretization of the advection operator. The collision integral and pressure gradient terms are not considered here because they are treated as source terms in the RKDG framework and the latter is specific only to problems with an applied pressure gradient. The performance metric is the average running time per RKDG timestep, which includes 3 Runge-Kutta stages of evaluating the volume and surface residuals, solving for $\frac{\partial \hat{f}^d_{\Omega,i}}{\partial t}$ and integrating it in time. A total of 10^5 elements is used, with 10 elements for each dimension. The algorithms in comparison deviate only in the evaluation of the sum-factorized integrals for the volume and surface residual in equations 3.29 and 3.38 respectively, where one uses the analytical forms derived and the other uses Gaussian quadrature. The results in Table 3.1 show that the proposed algorithms perform better than that based on quadrature. Higher performance improvements are also observed at higher polynomial order p.

Next, the tests described above are repeated including the evaluation of five hydrodynamic quantities, namely the number density n, bulk flow velocities u_1 and u_2 and stresses P_{11} and P_{22}, at $(p+3) \times (p+3)$ points within every physical space element. To evaluate the hydrodynamic quantities, the proposed algorithm utilizes the derived analytical moments of Legendre polynomials and the equilibrium Maxwell-Boltzmann distribution f^{MB} described in section 3.2.9 while the control algorithm applies Gaussian quadrature and sum factorization directly on integrals of f^{MB} and the discretized deviational distribution f^d. The results in table 3.2 reveal that the proposed algorithm added less than 10% to the original run times shown in table 3.1 while that based on quadrature increased its original run-time by about a factor of 4. Although the hydrodynamic quantities need not be generated at every time-step, it would be useful to generate all required quantities sufficiently frequently at minimal cost so that a running average could be performed over one unit of dimensionless time to reduce statistical "noise" from the collision integral. The proposed algorithm is able to accomplish this with both speed and accuracy as the moments of Legendre

polynomials and f^{MB} are evaluated exactly, which reduces the error of the algorithm down to discretization errors of f^d in time and space.

Polynomial Order p	Run Time (s)		Factor of Improvement
	Quadrature	Analytical	
1	22.14	9.420	2.35
2	187.5	68.55	2.74
3	877.9	291.3	3.01

Table 3.1: Running time per RKDG timestep for 10^5 elements – collisionless, no hydrodynamic quantities computed.

Polynomial Order p	Run Time (s)		Factor of Improvement
	Quadrature	Analytical	
1	88.76	10.35	8.58
2	745.1	73.76	10.1

Table 3.2: Running time per RKDG timestep for 10^5 elements – collisionless, hydrodynamic quantities computed.

Polynomial Order p	Run Time (s)		Factor of Improvement
	Quadrature	Analytical	
1	121.5	106.3	1.14
2	2413	2314	1.04

Table 3.3: Running time per RKDG timestep for 10^5 elements – with collisions using 10^3 particles, no hydrodynamic quantities computed.

Finally, a test is performed on the full Boltzmann equation with the collision integral term, but without evaluating the pressure gradient term and hydrodynamic quantities. The results in table 3.3 indicate that the collision integral is about 10 times more expensive to compute than the advection operator terms under the proposed algorithm for $p = 1$. Although the performance improvements achieved for the advection operator terms might seem futile when the collision integral is evaluated in full, they will come in useful during steady-state applications where "fast collisions" can be performed until the solution is sufficiently near steady state before evaluating the collision integral in full. The "fast collisions" are implemented by evaluating the

Polynomial Order p	Run Time (s)		Factor of Improvement
	Quadrature	Analytical	
1	31.38	18.55	1.69
2	241.7	122.3	1.98

Table 3.4: Running time per RKDG timestep for 10^5 elements – with fast collisions using 10^3 particles, no hydrodynamic quantities computed.

collision integral using a piece-wise constant approximation, which is comparable in cost to computing the advection operator terms, as shown in table 3.4. It should be noted that the running times per RKDG time-step presented in tables 3.3 and 3.4 correspond to evaluating the collision integral with 10^3 particles, using the variance-reduced, statistical sampling method developed in [9, 10]. The running times would increase further when more particles are necessary to reduce the statistical "noise" in the solution and ensure the stability of the RKDG method.

The results in this section demonstrate the effectiveness of the proposed algorithms in evaluating the advection operator terms and the hydrodynamic fields over those based on quadrature. Although the algorithms developed rely on a rectangular grid and a tensor product basis, this choice of spatial discretization is the most natural for the velocity space. If necessary, the physical space can be discretized using a nodal basis on an unstructured mesh to handle complex geometries while the velocity space can be discretized separately using a tensor product basis on a rectangular grid. This allows the algorithms developed for evaluating the hydrodynamic quantities to remain applicable as they only involve integration in velocity space. Furthermore, by expressing the basis function for f^d as $\phi_i(\mathbf{x}, \mathbf{c}) = g(\mathbf{x}) \prod_{i=1}^{3} \psi(c_i)$ where $g(\mathbf{x})$ is a general polynomial involving all the spatial dimensions, sum factorization can still be applied to factor out the integrals over the velocity space dimensions in the evaluation of the volume and surface residuals. These integrals can be evaluated using the derived analytical expressions in sections 3.2.5 and 3.2.6 to minimize computation cost. Only the integrals involving $g(\mathbf{x})$ over the physical space dimensions require evaluation via Gaussian quadrature.

Chapter 4

Convergence Test on a Problem with a Continuous Solution

This chapter investigates the physical space convergence properties of the RKDG method when implemented in 2 spatial dimensions for a simple test problem with a continuous solution. The choice of a test problem with a continuous solution allows a meaningful comparison of the spatial convergence rates with known theoretical predictions to validate our RKDG implementation. The following two sections present the implementation and convergence results for sinusoidal waves propagating separately in each of the spatial dimensions, as well as simultaneously in 2 spatial dimensions.

4.1 Propagation of Sinusoidal Wave in 1 Spatial Dimension

4.1.1 Formulation and Implementation

Consider a single sinusoidal wave propagating along the x_i direction from $x_{i,min}$ to $x_i = x_{i,max}$ with dimensionless speed $|c_i| = \frac{2}{\sqrt{\pi}}$. This wave can be described by a simplified "collisionless Boltzmann" equation (see equation 2.19 for the complete

equation)

$$\begin{aligned} \frac{\partial f}{\partial t} + \frac{\sqrt{\pi}}{2}\mathbf{c} \cdot \frac{\partial f}{\partial \mathbf{x}} &= 0 \\ \Rightarrow \qquad \frac{\partial f}{\partial t} + \frac{\partial f}{\partial x_i} &= 0 \end{aligned} \tag{4.1}$$

and a time-dependent boundary condition

$$f(x_1, x_2, t)|_{x_i = x_{i,min}} = 0.1 \sin\left(2\pi\left(t - x_{i,min}\right)\right) \tag{4.2}$$

Using the method of characteristics, the analytical solution to the above problem is found to be

$$f(x_1, x_2, t) = 0.1 \sin\left(2\pi\left(t - x_i\right)\right) \tag{4.3}$$

where the index i depends on the direction of wave propagation x_i. Note that the function f is independent of the other spatial dimensions, except x_i. Furthermore, boundary conditions need not be specified at the other domain boundaries, except $x_i = x_{i,min}$, since boundary fluxes are only propagated into the domain through that boundary.

This test problem is implemented for disturbances propagating along the x_1 and x_2 directions separately. Spatial discretization is performed as described in section 3.2.1 only on the 2 physical space dimensions. The velocity space only consists of a single node centered at $\mathbf{c} = [\frac{2}{\sqrt{\pi}}\ 0\ 0]$ if $i = 1$, or $\mathbf{c} = [0\ \frac{2}{\sqrt{\pi}}\ 0]$ if $i = 2$. Time discretization is performed using the 3^{rd} order Runge-Kutta (RK3) method described in section 3.2.2 except that the time-step is determined, based on the CFL condition in equation 3.19, using $0.5CFL_{L^2}$ instead of CFL_{L^2} to minimize the effect of time-discretization errors corrupting the spatial convergence rates.

Only the volume and surface residuals are evaluated, as described in sections 3.2.5 and 3.2.6 respectively. The dynamic boundary conditions are evaluated at the correct

times during each intermediate Runge-Kutta stage as follows [18]

$$f(x_1, x_2, t_k)\big|_{x_i = x_{i,min}} = 0.1 \sin\left(2\pi\left(t_k - x_{i,min}\right)\right) \tag{4.4}$$

$$f^{(1)}\big|_{x_i = x_{i,min}} = 0.1 \sin\left(2\pi\left(\left(t_k + \Delta t_k\right) - x_{i,min}\right)\right) \tag{4.5}$$

$$f^{(2)}\big|_{x_i = x_{i,min}} = 0.1 \sin\left(2\pi\left(\left(t_k + \frac{\Delta t_k}{2}\right) - x_{i,min}\right)\right) \tag{4.6}$$

The output of interest is the discretized approximation f_h of the function f, which can be reconstructed from the evaluated modal coefficients $\hat{f}_{h\Omega,i}$ and basis functions ϕ_i using the same method described in equations 3.5 and 3.21. The error associated with the RKDG discretization is measured as the functional L^2 norm of the steady state difference between the analytical solution f and its discretized approximation f_h, which is given by

$$\|f - f_h\|_{L^2} = \sqrt{\int_{x_{1,min}}^{x_{1,max}} \int_{x_{2,min}}^{x_{2,max}} (f - f_h)^2 dx_1 dx_2} \tag{4.7}$$

and evaluated using Gaussian quadrature with $p + 2$ quadrature points per spatial dimension in each element.

4.1.2 Convergence Results for 1D Wave Propagation

Table 4.1 presents the L^2 errors for different polynomial orders p of the DG approximation and different levels of spatial discretization. Only one set of results for waves propagating in the x_1 direction is presented as the other test case yields similar results. The convergence rates presented in table 4.1 for each level of spatial discretization are determined based on the error corresponding to the previous spatial discretization level.

Since the analytical solution f to this problem is a continuous sinusoid, the optimal rate of spatial convergence for the L^2 error can be shown to be $p + 1$ [19]. Hence, under an RK3 time integration scheme, the L^2 error of the RKDG solution for this

Polynomial Order p	**♯ Elements** $\frac{1}{\Delta x_i}$	**Error** $\|f - f_h\|_{L^2}$	**Order of Convergence**
0	10	4.3173e-02	-
	20	2.9408e-02	0.5539
	40	1.7502e-02	0.7487
	80	9.5844e-03	0.8687
	160	5.0174e-03	0.9338
1	10	2.6934e-02	-
	20	7.0136e-03	1.9412
	40	1.7537e-03	1.9997
	80	4.3728e-04	2.0038
	160	1.0912e-04	2.0027
2	10	8.6103e-05	-
	20	1.0734e-05	3.0039
	40	1.3421e-06	2.9996
	80	1.6808e-07	2.9973
	160	2.1099e-08	2.9939
3	10	4.2504e-03	-
	20	2.6172e-04	4.0215
	40	1.6220e-05	4.0122
	80	1.0113e-06	4.0035
	160	6.3225e-08	3.9996

Table 4.1: Spatial convergence results for 1D disturbance propagation

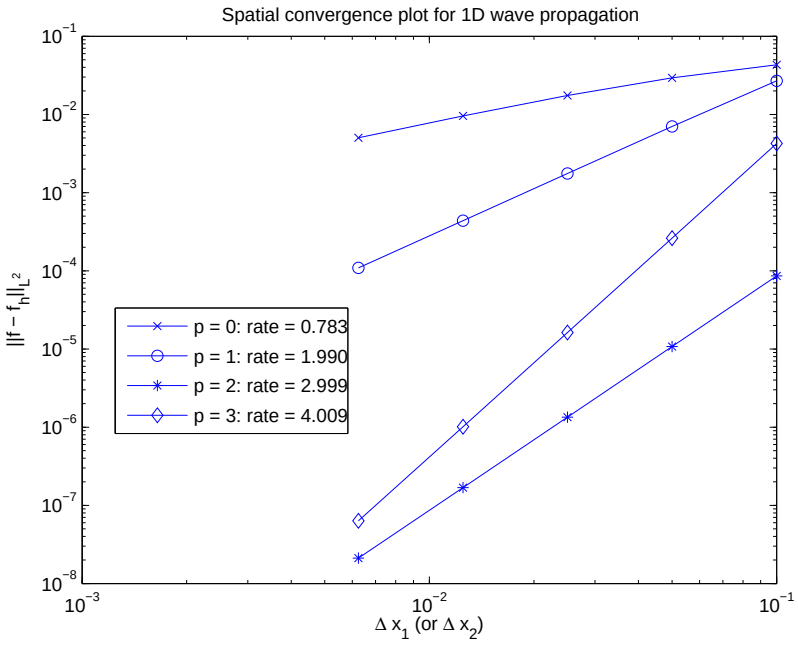

Figure 4-1: Spatial convergence plot for 1D wave propagation

problem can be given, asymptotically, by [19, 8, 18]

$$\|f - f_h\|_{L^2} = K_1 \Delta x_i^{p+1} + K_2 \Delta t^3 = K_1 \Delta x_i^{p+1} + K_2' \Delta x^3 \tag{4.8}$$

since Δt is determined in proportion to Δx based on the CFL condition. Hence, with parameters chosen such that the first term dominates, the convergence rate is expected to be close to $p+1$. This agrees with the convergence rates obtained for the test problem up to $p = 3$, as shown in table 4.1. Although the convergence rates observed for $p = 0$ deviate significantly from $p+1$ at low levels of spatial discretization, this could be due to significant time-discretization errors from the large time-steps used, which are in proportion to the element size. The convergence rate is clearly observed to approach the theoretical value of $p+1$ for $p = 1$ as the spatial discretization becomes finer. For $p \geq 2$, the convergence rates are very close to $p+1$ but exhibit a slight decrease with decreasing element sizes. This could be attributed to the spatial discretization error term in equation 4.8 becoming smaller and losing dominance over the time discretization error term at finer spatial discretizations.

4.2 Propagation of Sinusoidal Waves in 2 Spatial Dimensions

4.2.1 Formulation and Implementation

The phenomenon of 2 sinusoidal waves propagating simultaneously in the x_1 and x_2 directions with speeds $|c_1| = |c_2| = \frac{2}{\sqrt{\pi}}$ can be described by the following simplified form of the collisionless Boltzmann equation

$$\frac{\partial f}{\partial t} + \sum_{i=1}^{2} \frac{\partial f}{\partial x_i} = 0 \tag{4.9}$$

and the time-dependent boundary conditions

$$f(x_1, x_2, t)|_{x_i = x_{i,min}} = 0.1 \sin\left(2\pi\left(t - x_{i,min}\right)\right) \quad (i = 1, 2) \tag{4.10}$$

Using the method of characteristics and the principle of superposition, the analytical solution to the above problem is derived as

$$f(x_1, x_2, t) = \sum_{i=1}^{2} 0.1 \sin\left(2\pi\left(t - x_i\right)\right) \tag{4.11}$$

Spatial discretization is performed as described in section 3.2.1 but the velocity space only consists of a single node centered at $\mathbf{c} = [\frac{2}{\sqrt{\pi}}\ \frac{2}{\sqrt{\pi}}\ 0]$. Time discretization, boundary condition evaluation and error measurement are the same as that described in the previous section, 4.1.

4.2.2 Convergence Results for 2D Wave Propagation

The results obtained in table 4.2 show that the convergence rates for $p = 0$ and $p = 1$ in this problem approach the theoretical value of $p+1$ with finer spatial discretization. Similar to the 1D wave propagation problem, the convergence rate for $p = 2$ is very close to its theoretical value but decreases slightly with decreasing element sizes due

Polynomial Order p	**♯ Elements** $\frac{1}{\Delta x_i}$	**Error** $\|f - f_h\|_{L^2}$	**Order of Convergence**
0	10	5.2096e-02	-
	20	3.2923e-02	0.6621
	40	1.9014e-02	0.7920
	80	1.0305e-02	0.8838
	160	5.3902e-03	0.9349
1	10	2.3060e-02	-
	20	6.1551e-03	1.9056
	40	1.5589e-03	1.9812
	80	3.9015e-04	1.9984
	160	9.7436e-05	2.0015
2	10	1.2141e-04	-
	20	1.5180e-05	2.9996
	40	1.9013e-06	2.9972
	80	2.3868e-07	2.9938
	160	3.0095e-08	2.9875

Table 4.2: Spatial convergence results for 2D disturbance propagation

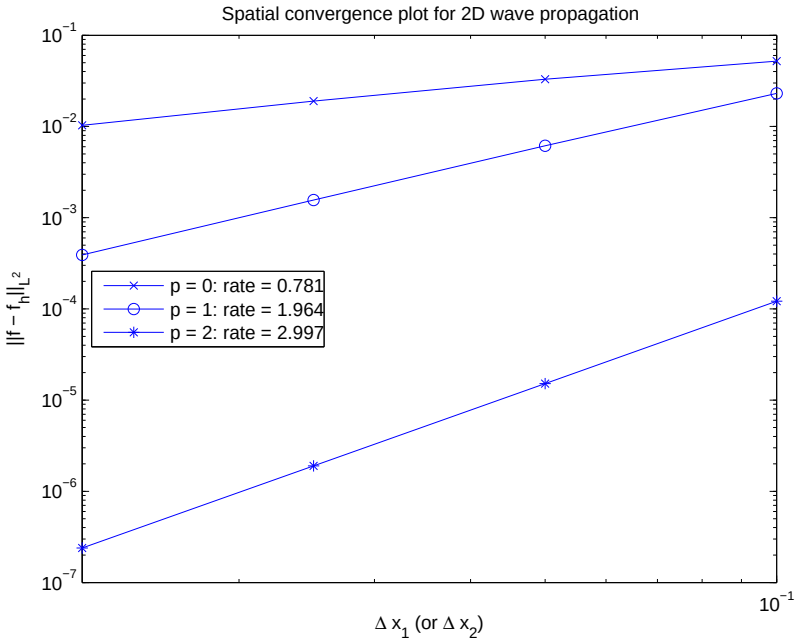

Figure 4-2: Spatial convergence plot for 2D wave propagation

to the same reason described in section 4.1.2.

The convergence results in this and the previous section verify the high-order convergence of the RKDG method, which also confirms that our RKDG implementation is correct, at least in the physical space dimension.

Chapter 5

Pressure Driven Flow Problem

This chapter presents the RKDG solutions of the pressure driven flow problem described in section 2.2 for various Knudsen numbers (Kn) and aspect ratios (AR). The first section presents specific implementation details of the variance-reduced RKDG method for this test problem. Next, results from a convergence test in the collisionless limit ($Kn = \infty$) for an aspect ratio $AR = 2$ are presented to reveal the effects of spatial discretization, velocity space truncation and polynomial order on the steady state error. The last section presents the steady state velocity profiles and non-dimensional mass flux Q_p obtained for $Kn = 0.2, 1$ and 10 for $AR = 1, 2$ and 4. The non-dimensional mass flux obtained in the convergence test and the last section are validated against results obtained by Sone and Hasegawa [14].

5.1 Implementation

The variance-reduced RKDG method is implemented as described in chapter 3, except that only 2 physical space dimensions (x_1 and x_2) and 3 velocity space dimensions are involved. The symmetry boundary conditions described in section 2.2 are specified directly on the deviational distribution f^d as required by equations 2.33 and 2.34

$$x_1 = 0: \quad f^d(x_1, x_2, c_1, c_2, c_3, t) = f^d(x_1, x_2, -c_1, c_2, c_3, t) \tag{5.1}$$

$$x_2 = 0: \quad f^d(x_1, x_2, c_1, c_2, c_3, t) = f^d(x_1, x_2, c_1, -c_2, c_3, t) \tag{5.2}$$

to reduce the physical space computational domain to the positive quadrant $0 \leq x_i \leq x_{i,max}$ $(i = 1, 2)$. A truncated velocity space $-4 \leq c_i \leq 4$ $(i = 1$ to $3)$ is used in the interest of computational efficiency, as justified in section 3.1.1. In addition, the velocity space is meshed non-uniformly such that element sizes are smallest around $\mathbf{c} = 0$, with a ratio of 8 between the largest and smallest element edge.

One of the test metrics used for this problem is the non-dimensional mass flux, which is defined as

$$Q_p = \frac{2Kn\sqrt{\pi}}{\kappa}\bar{u} \tag{5.3}$$

where the Knudsen number (Kn) is as defined in equation 2.31, $\kappa = 10^{-4}$ is the applied pressure gradient and $\bar{u} = \bar{u}_3$ is the average flow velocity across the channel cross-section along the x_3 direction, which can be computed as

$$\begin{aligned} \bar{u} &= \frac{\int c_3 \, f \, d^3\mathbf{c} \, d^2\mathbf{x}}{A} \\ &= \frac{16J}{A} \sum_{\Omega} \left(2c_{3_\Omega} \hat{f}^d_{\Omega,0,0,0,0,0} + \frac{\Delta c_{3_{\Omega_c}}}{3} \hat{f}^d_{\Omega,0,0,0,0,1} \right) \end{aligned} \tag{5.4}$$

by extending the algorithm for evaluating the bulk flow velocity in section 3.2.9. The area A corresponds to the area of the computational domain, which is 1/4 of the channel cross-sectional area. To compute the volume Jacobian J in this problem, equation 3.24 should be modified for the case of a 5 dimensional phase space. Furthermore, the modal coefficient tensor $\hat{f}^d$ is now a 6-dimensional tensor for the case of a 5-dimensional phase space.

5.2 Convergence Test in Collisionless Limit

This section investigates the convergence of the variance-reduced RKDG method in the collisionless limit $(Kn = \infty)$ by solving the collisionless Boltzmann equation for $Kn = 1$, $AR = 2$. The mass flux Q_p computed by Sone and Hasegawa [14] in the collisionless limit will be used as a reference for computing the error in our RKDG solution. Although the solutions of Sone and Hasegawa are based on the

linearized Boltzmann-Krook-Welander (BKW) equation, the steady state results in the collisionless limit are expected to be the same as that from solving our collisionless Boltzmann equation. Table 5.1 shows the steady state RKDG solution Q_p and the corresponding percentage error under different discretization levels of the physical and velocity space, different ranges of the truncated velocity space, as well as different polynomial orders p of the RKDG solution. Figures 5-1 and 5-2 show the temporal convergence of the RKDG solution Q_p while table 5.2 shows the dimensionless time ($\tau = \bar{t}^*$ in equation 2.15) and running time required to reach steady state under the different conditions mentioned above.

Polynomial Order p	**Spatial Discretization** $n_{x_1} \times n_{x_2} \times n_{c_1} \times n_{c_2} \times n_{c_3}$	**Velocity Space**	**Dimensionless Mass Flux** Q_p	**Error (%)**
1	$5 \times 5 \times 10 \times 10 \times 10$	$[-4,\ 4]$	2.249155	-2.423
1	$10 \times 10 \times 10 \times 10 \times 10$	$[-4,\ 4]$	2.249240	-2.419
1	$5 \times 5 \times 20 \times 20 \times 20$	$[-4,\ 4]$	2.280538	-1.061
1	$5 \times 5 \times 20 \times 20 \times 20$	$[-3,\ 3]$	2.285597	-0.842
2	$5 \times 5 \times 10 \times 10 \times 10$	$[-3,\ 3]$	2.286118	-0.819
Sone and Hasegawa [14]			2.305	0

Table 5.1: Steady state solution and error for Q_p in pressure driven flow problem at $Kn = \infty$

Order p	**Spatial Discretization**	**Velocity Space**	**Time to Steady State(τ)**	**Steps Needed**	**Running Time (s) per Step**	**Total Running Time (hr)**
1	$5^2 \times 10^3$	$[-4,\ 4]$	~ 30	3190	3.2	2.8
1	$10^2 \times 10^3$	$[-4,\ 4]$	~ 30	6380	11.5	20.4
1	$5^2 \times 20^3$	$[-4,\ 4]$	~ 60	6380	25.7	45.5
1	$5^2 \times 20^3$	$[-3,\ 3]$	~ 80	6380	25.7	45.5
2	$5^2 \times 10^3$	$[-3,\ 3]$	~ 75	9970	30.8	85.3

Table 5.2: Time to steady state in pressure driven flow problem at $Kn = \infty$

The results in the first three rows of table 5.1 show that a factor of 2 refinement in every dimension of the velocity space achieved a significantly greater reduction (56% compared to 0.2%) in the steady state error compared to a similar refinement in the physical space. This is consistent with the distribution function f having a

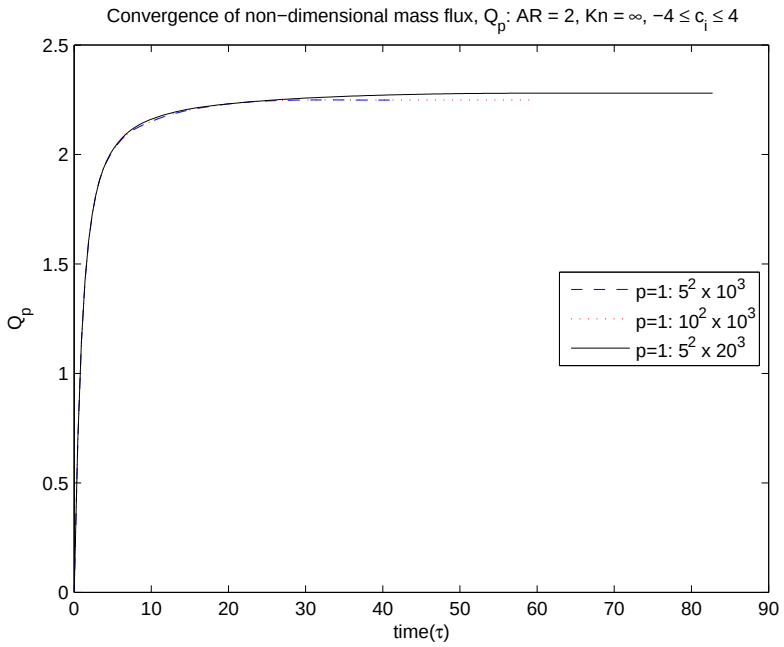

Figure 5-1: Effect of physical and velocity space discretization on the temporal convergence of the non-dimensional mass flux Q_p

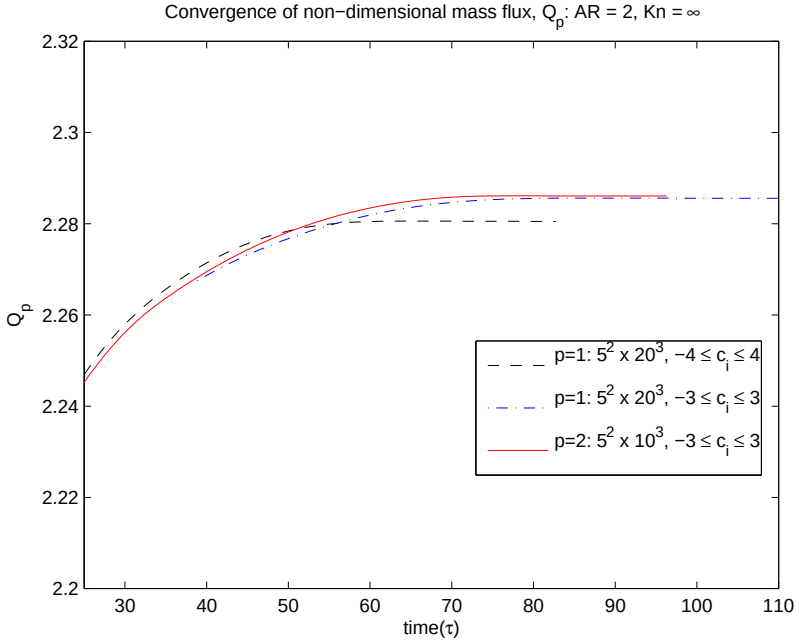

Figure 5-2: Effect of truncated velocity space and polynomial order on the temporal convergence of the non-dimensional mass flux Q_p

discontinuity and large gradients near $\mathbf{c} = 0$, as well as having very little variation over the physical space in the collisionless limit [20]. By truncating the velocity space further from $[-4,\ 4]$ to $[-3,\ 3]$ while retaining the discretization level, the elements will be smaller and a piecewise linear ($p = 1$) RKDG solution will be able to describe the large variations in f near $\mathbf{c} = 0$ more accurately over each element. This is evidenced in the 3^{rd} and 4^{th} rows of table 5.1 where the steady state error is reduced from 1.061% to 0.842%. Furthermore, there is no increase in the computational time as shown in the corresponding rows of table 5.2.

A similar (slightly lower) steady state error can also be achieved using a piecewise quadratic ($p = 2$) RKDG approximation over a velocity space mesh that is a factor of 2 coarser in every dimension as shown in the last row of table 5.1. Although the dimensionless time to steady state, expressed in terms of the characteristic timescale $\tau = \bar{t}^*$ defined in equation 2.15, for the $p = 2, 5^2 \times 10^3$ test case is slightly less than that for the $p = 1, 5^2 \times 20^3$ test case, the total running time is almost twice as long due to a 40% smaller timestep imposed by the CFL_{L^2} used, as defined in equation 3.20. Hence, for the same level of accuracy, using a $p = 1$ approximation with a finer discretization near regions of discontinuities or large variations in f is still more practical than going to a higher order $p = 2$ approximation.

The steady state non-dimensional mass flux Q_p in the collisionless limit ($Kn = \infty$) is also obtained for aspect ratios $AR = 1$ and 4, and are presented in table 5.3 together with that for $AR = 2$. The results presented for all three aspect ratios correspond to using a $p = 1$ polynomial approximation and a truncated velocity space $c_i\ \epsilon\ [-3,\ 3]$ ($i = 1$ to 3) since this is optimal in terms of both speed and accuracy.

5.3 Steady State Pressure Driven Flow with Collisions

In this section, we discuss our results in the presence of collisions. To our knowledge, no simulation data for the full Boltzmann equation based on the hard sphere model exists. Hence, we will use the Boltzmann-Krook-Welander(BKW) results of Sone and Hasegawa as a rough guide, as explained in section 5.3.2.

5.3.1 Velocity Profiles

Figures 5-3, 5-4 and 5-5 show the steady state bulk flow velocity (u_3) profile across the positive quadrant of the channel cross-section for aspect ratios of 1, 2 and 4 respectively. Results are shown for Knudsen numbers $Kn = 10, 1$ and 0.2 under each aspect ratio. The parabolic profiles observed across the x_1 and x_2 axes are consistent with the Poiseuille nature of the expected solution and qualitatively validates our implemented variance-reduced RKDG method.

5.3.2 Steady State Results of Non-dimensional Mass Flux

In this section, the non-dimensional mass flux Q_p obtained from solving the full Boltzmann equation based on the hard sphere model for $Kn = 0.2, 1$ and 10 under $AR = 1, 2$ and 4 is presented and validated against results by Sone and Hasegawa [14], as shown in table 5.3. Note that in the paper by Sone and Hasegawa [14], the Knudsen number is defined to be twice of that defined in this thesis. Furthermore, their results correspond to solutions of the linearized Boltzmann-Krook-Welander(BKW) equation, which is different from solutions of the full Boltzmann equation for finite Knudsen numbers. Hence, a comparison between solutions of the 2 models may be performed by comparing the hard sphere results we obtain for Knudsen number Kn to the BKW results at a Knudsen number of $1.27Kn$ [21]. The BKW results were obtained by linearly interpolating the results of Sone and Hasegawa [14].

For all the test cases involving collisions ($Kn \neq \infty$), the number of collision

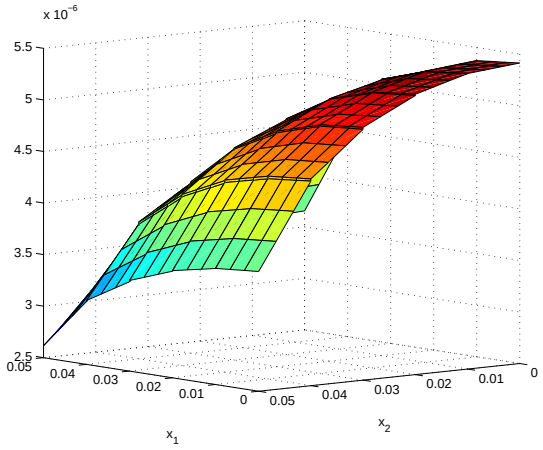

a. $Kn = 10$

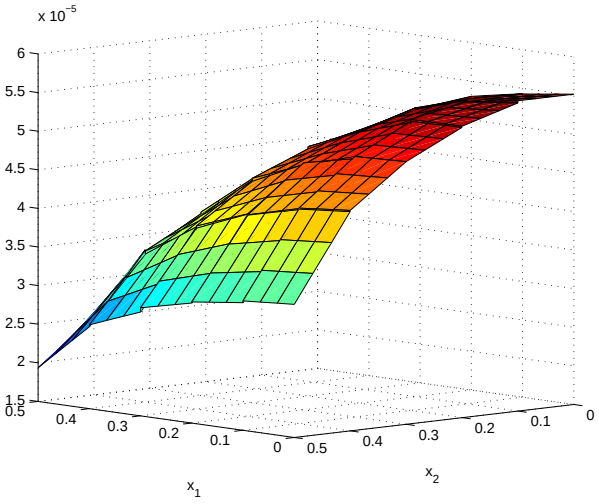

b. $Kn = 1$

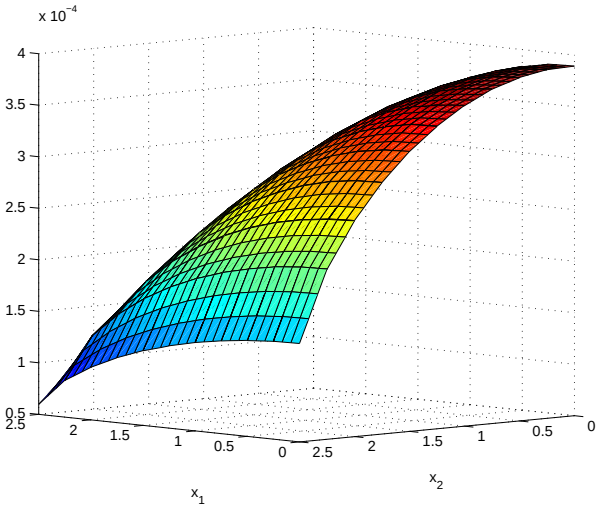

c. $Kn = 0.2$

Figure 5-3: Non-dimensional flow velocity u_3 (AR = 1)

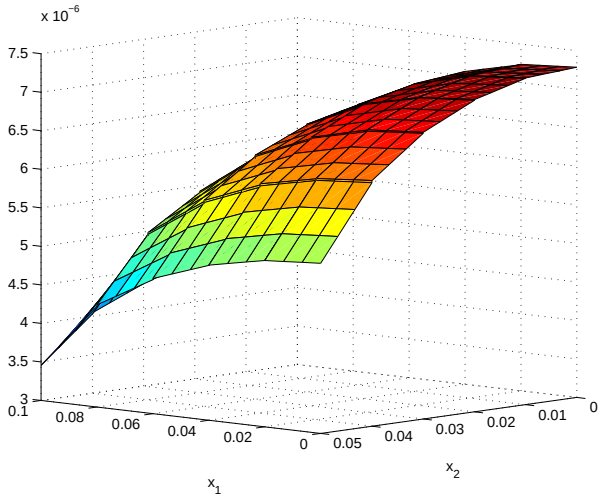

a. $Kn = 10$

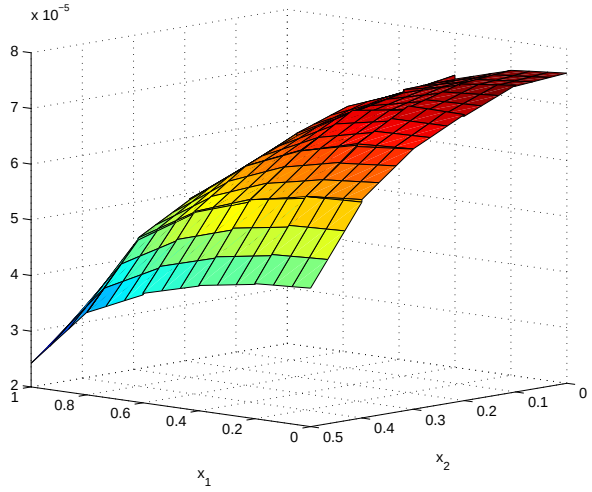

b. $Kn = 1$

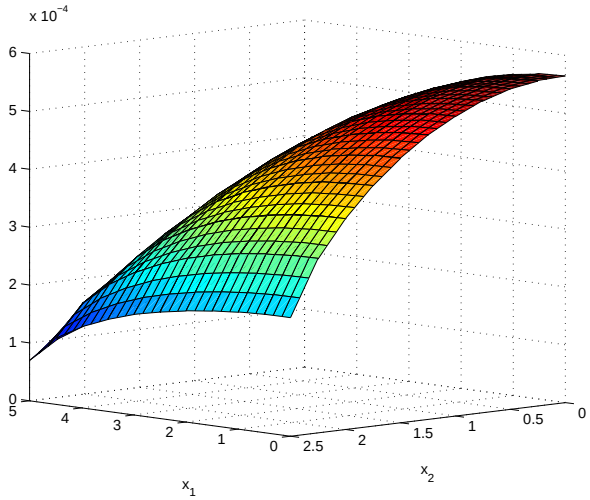

c. $Kn = 0.2$

Figure 5-4: Non-dimensional flow velocity u_3 (AR = 2)

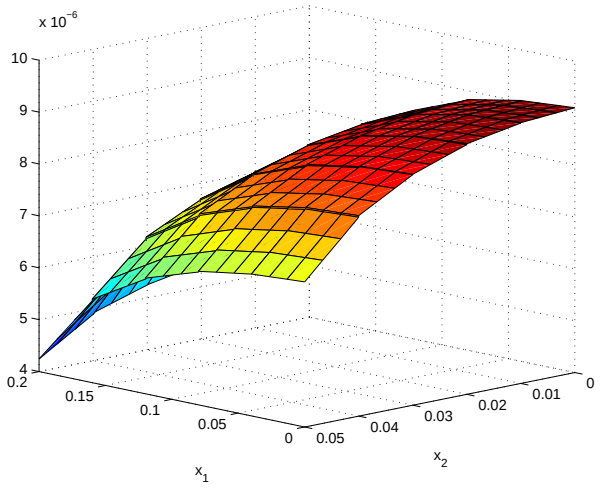

a. $Kn = 10$

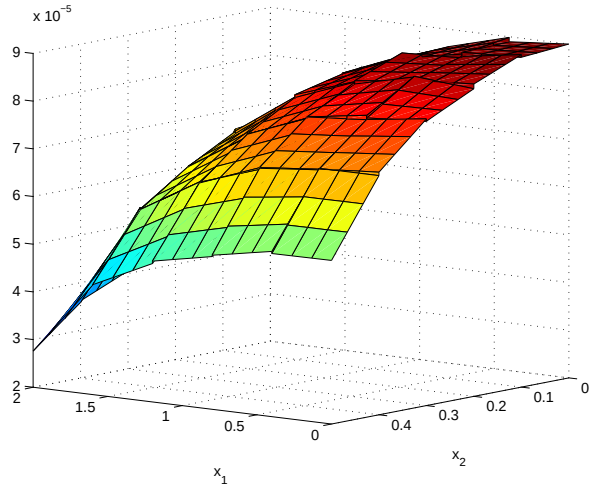

b. $Kn = 1$

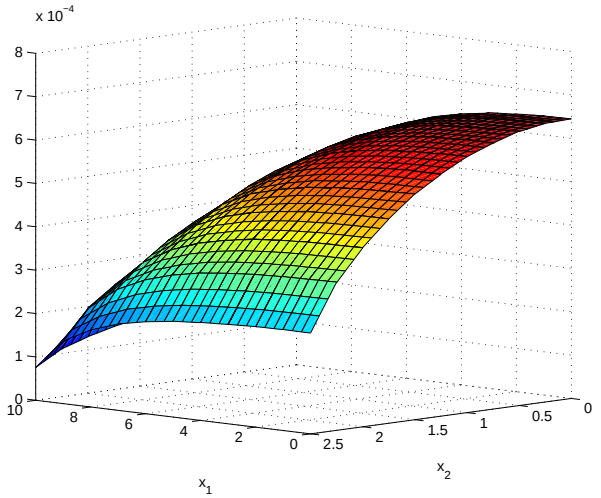

c. $Kn = 0.2$

Figure 5-5: Non-dimensional flow velocity u_3 (AR = 4)

samples N_c used to evaluate the collision integral are chosen primarily for numerical stability and are as shown in table 5.3. Furthermore, the variance-reduced RKDG method is implemented to perform "fast" collisions until the solution is observed to be reasonably close to steady state before switching to evaluating the weak form collision integral term in full. The "fast" collision algorithm evaluates the weak form collision integral term in equation 3.9 using a piecewise constant ($p = 0$) approximation, which allows a significant reduction in the computational cost. Details of evaluating the collision integral can be found in [9, 10].

The velocity space discretization chosen for $Kn = 1$ is coarser than that for $Kn = 10$ because at lower Kn, the distribution function has a weaker discontinuity at $\mathbf{c} = 0$ and will be a smoother function of velocity [20]. Next, the physical space discretization chosen for $Kn = 0.2$ is finer than that for $Kn = 1$ and 10 because at low Kn, the distribution function will have significantly more spatial variation [20]. The time-steps used for all the test cases are determined based on the CFL condition shown in equations 3.19 and 3.20. The only exception is the test case of $Kn = 0.2, AR = 1$ which uses $0.5{CFL_L}^2$ instead of CFL_{L^2} to determine the time-step because the latter results in numerical instability if used with $N_c = 10^5$ collision samples.

The results in table 5.3 indicate a good match between the obtained dimensionless mass flux Q_p and that reported by Sone and Hasegawa, which validates the implemented variance-reduced RKDG method for solving the full Boltzmann equation. Furthermore, the mass flux Q_p that we obtained are lower than that reported by Sone and Hasegawa for all test cases, which is consistent with the behavior of solutions obtained from the full Boltzmann equation based on the hard sphere model and that from the linearized BKW equation [21]. Although the test cases at all Kn exhibit an increasing error with the aspect ratio (AR), this can be attributed to increasing spatial discretization errors from meshing the increasing x_1 dimension with the same number of elements for each Kn.

Kn	Order p, Collision Samples N_c, Spatial Discretization, Velocity Space	AR	Dimensionless Mass Flux Q_p		Error (%)
			RKDG	Sone and Hasegawa [14]	
∞	$p = 1$, Collisionless	1	1.67	1.677	-0.51
	$5^2 \times 20^3$	2	2.29	2.305	-0.84
	$c_i \, \epsilon \, [-3, \, 3]$	4	2.96	3.002	-1.28
10	$p = 1$, $N_c = 10^3$	1	1.59	1.589	-0.25
	$5^2 \times 20^3$	2	2.14	2.151	-0.33
	$c_i \, \epsilon \, [-4, \, 4]$	4	2.70	2.715	-0.41
1	$p = 1$, $N_c = 10^3$	1	1.52	1.537	-0.87
	$5^2 \times 10^3$	2	2.06	2.087	-1.30
	$c_i \, \epsilon \, [-4, \, 4]$	4	2.49	2.533	-1.62
0.2	$p = 1$, $N_c = 10^5$	1	1.88	1.898	-0.83
	$10^2 \times 10^3$	2	2.68	2.709	-0.93
	$c_i \, \epsilon \, [-4, \, 4]$	4	3.21	3.249	-1.28
0.1	$p = 1$, $N_c = 10^5$				
	$10^2 \times 10^3$	2	3.64	3.739	-2.76
	$c_i \, \epsilon \, [-4, \, 4]$				

Table 5.3: Steady state solution and error for Q_p in pressure driven flow problem at various Knudsen numbers (Kn)

Chapter 6

Conclusions

The variance-reduced RKDG method has been implemented to solve the Boltzmann equation in 2 physical space and 3 velocity space dimensions using an alternative algorithm for evaluating the advection operator terms and hydrodynamic quantities of interest. Compared to a standard sum factorization algorithm based on Gaussian quadrature, the alternative algorithms are able reduce the RKDG computational cost for the advection operator terms by a factor of 2.3 to 3 by making use of analytical expressions for the inner products and moments of Legendre polynomials. When the output hydrodynamic quantities are computed, a overall factor of 8.5 to 10 reduction in the computational cost can be achieved. Although the collision integral term takes about 10 times longer to evaluate than the advection operator terms, a piecewise constant approximation can be used to significantly reduce the collision integral computational cost while the solution is not yet close to steady state. This would allow the performance benefits of the proposed algorithms to be reaped while not affecting the accuracy of the steady state solution.

The high order convergence in physical space of the present RKDG implementation has been verified using a simple test problem with a continuous analytical solution.

When the variance-reduced RKDG method is applied to the pressure driven flow test problem, the computed dimensionless mass flux Q_p shows good agreement (underestimation of 0.5% to 1.2%) with that reported by Sone and Hasegawa [14] in the

collisionless limit ($Kn = \infty$) for aspect ratios $AR = 1, 2$ and 4. For $Kn = 10, 1$ and 0.2, the results show good agreement with those obtained by Sone and Hasegawa from solutions of the linearized Boltzmann-Krook-Welander(BKW) equation, provided they are compared at the "equivalent" Knudsen number of $1.27Kn$. These results verify the accuracy of the implemented variance-reduced RKDG method in solving the full Boltzmann equation under multiple spatial dimensions.

Although it has been found that using a piecewise quadratic ($p = 2$) discretization for the RKDG solution yields slightly more accurate results than a piecewise linear ($p = 1$) discretization at twice the spatial resolution in each velocity space dimension for $Kn = \infty$, the computation time for the latter is still about 2 times shorter than the former. The main reason is a smaller CFL, and thus time-step, required for the $p = 2$ calculation. Hence, for this specific test problem and implementation of the variance-reduced RKDG method, it would be more efficient to pursue better accuracy by using a $p = 1$ scheme with a finer spatial discretization than to utilize a higher order $p = 2$ scheme with a coarser spatial discretization. This can be achieved using a combination of finer spatial discretization and non-uniform spacing to generate more elements near regions of discontinuities or large variations in the distribution function.

6.1 Recommendations for Future Work

6.1.1 Unique Discretization in Physical and Velocity Space

The algorithms developed in this thesis for evaluating the advection operator terms and hydrodynamic quantities require rectangular spatial elements and a tensor product basis for the distribution function f. This choice of spatial meshing and basis is most natural for the velocity space and is extremely efficient in computing moments of the distribution function in velocity space to evaluate the spatially dependent hydrodynamic quantities. However, it is not necessary to impose the same meshing and basis on every spatial dimension. One possible area of future work is to perform physical space discretization using an unstructured mesh to handle complex physical

geometries, and a nodal basis for f to reduce the number of basis functions from $(p+1)^2 \times (p+1)^3$ to $2(p+1) \times (p+1)^3$ in the case of 2 physical and 3 velocity space dimensions with an order p discretization. The velocity space can still be discretized with rectangular elements and a tensor product basis to retain the use of sum factorization of integrals over the velocity space and the computational advantage of the developed algorithms in evaluating the hydrodynamic quantities and part of the advection operator terms. However, modifications would have to be made to compute the integrals over physical space using Gaussian quadrature. It would also be of interest to note if the reduction in computational cost for the collision integral and advection operator terms due to a smaller number of basis functions would be sufficient to offset to increase in cost from Gaussian quadrature.

6.1.2 Reduction in Computational Cost to Reach Steady State

Although this thesis has clearly demonstrated the feasibility of the RKDG approach for two physical space dimensions without the need for supercomputing facilities, further reducing the computational cost of the present approach is highly desirable. One aspect where significant potential for improvement exists is the solution of steady state problems, where explicit time-integration, especially for low Knudsen numbers, is very costly due to the long time required to reach steady state coupled to the (relatively) short timestep imposed by the CFL condition. To reduce the computational cost associated with reaching steady state, one could investigate the possibility of using a time stepping scheme that allows larger timesteps while maintaining stability. Alternatively, implicit steady state solution methods may need to be developed.

Appendix A

Legendre Polynomial Functions

A.1 Definition and Derivatives

The following are the Legendre polynomials of order up to $p = 6$.

$$\psi_0(\xi) = 1 \tag{A.1}$$

$$\psi_1(\xi) = \xi \tag{A.2}$$

$$\psi_2(\xi) = \frac{1}{2}\left(3\xi^2 - 1\right) \tag{A.3}$$

$$\psi_3(\xi) = \frac{1}{2}\left(5\xi^3 - 3\xi\right) \tag{A.4}$$

$$\psi_4(\xi) = \frac{1}{8}\left(35\xi^4 - 30\xi^2 + 3\right) \tag{A.5}$$

$$\psi_5(\xi) = \frac{1}{8}\left(63\xi^5 - 70\xi^3 + 15\xi\right) \tag{A.6}$$

$$\psi_6(\xi) = \frac{1}{16}\left(231\xi^6 - 315\xi^4 + 105\xi^2 - 5\right) \tag{A.7}$$

The derivatives of Legendre polynomials can also be expressed in terms of lower order Legendre polynomials and derivatives as follows:

$$\frac{d\psi_0}{d\xi} = 0 \tag{A.8}$$

$$\frac{d\psi_1}{d\xi} = 1 = \psi_0(\xi) \tag{A.9}$$

$$\frac{d\psi_2}{d\xi} = 3\xi = 3\psi_1(\xi) \tag{A.10}$$

$$\frac{d\psi_3}{d\xi} = \frac{1}{2}\left(15\xi^2 - 3\right) = 5\psi_2(\xi) + 1 \tag{A.11}$$

$$\frac{d\psi_4}{d\xi} = \frac{1}{8}\left(140\xi^3 - 60\xi\right) = 7\psi_3(\xi) + 3\psi_1(\xi) \tag{A.12}$$

$$\frac{d\psi_5}{d\xi} = \frac{1}{8}\left(315\xi^4 - 210\xi^2 + 15\right) = 9\psi_4(\xi) + \frac{d\psi_3}{d\xi} \tag{A.13}$$

$$\frac{d\psi_6}{d\xi} = \frac{1}{16}\left(1386\xi^5 - 1260\xi^3 + 210\xi\right) = 11\psi_5(\xi) + \frac{d\psi_4}{d\xi} \tag{A.14}$$

A.2 Inner Products

The Legendre polynomials are orthogonal, which means that their inner products are given by

$$\Psi_{a\,b} = \int_{-1}^{1} \psi_b(\xi)\,\psi_a(\xi)\,d\xi = \frac{2}{2a+1}\delta_{ab} \tag{A.15}$$

where

$$\delta_{ab} = \begin{cases} 1 & \text{if } a = b \\ 0 & \text{otherwise} \end{cases} \tag{A.16}$$

and a,b are the orders (or degrees) of the Legendre polynomials ψ_a and ψ_b respectively.

Using the Legendre derivative expressions and orthogonality property defined above, it can be shown that the tensor Ψ'_{ab} of inner products involving Legendre polynomials and their derivatives possess a sparse, lower triangular, Toeplitz structure. The following shows the tensor Ψ'_{ab} for the case of Legendre polynomials and

derivatives up to order $p = 6$.

$$\Psi'_{ab} = \int_{-1}^{1} \psi_b \frac{d\psi_a}{d\xi_m} \, d\xi_m = \begin{bmatrix} 0 & 0 & \cdots & \cdots & \cdots & 0 & 0 \\ 2 & 0 & \ddots & \ddots & \ddots & \ddots & 0 \\ 0 & 2 & \ddots & \ddots & \ddots & \ddots & \vdots \\ 2 & 0 & \ddots & \ddots & \ddots & \ddots & \vdots \\ 0 & 2 & \ddots & \ddots & \ddots & \ddots & \vdots \\ 2 & 0 & 2 & 0 & 2 & 0 & 0 \\ 0 & 2 & 0 & 2 & 0 & 2 & 0 \end{bmatrix} \tag{A.17}$$

for $a, b = 0$ to 6

The first moment of the inner product of Legendre polynomials is given by [17]

$$\int_{-1}^{1} \xi \, \psi_b \, \psi_a \, d\xi = \begin{cases} \frac{2b}{(2b-1)(2b+1)} & \text{if } a = b-1 \\ \frac{2(b+1)}{(2b+1)(2b+3)} & \text{if } a = b+1 \\ 0 & \text{otherwise} \end{cases} \tag{A.18}$$

A.3 Moments in Space

The 0^{th} moment of the Legendre polynomials is given by

$$\int_{-1}^{1} \psi_k \left(\xi\right) d\xi = \begin{cases} 2 & \text{if } k = 0 \\ 0 & \text{otherwise} \end{cases} \tag{A.19}$$

The 1^{st} moment of the Legendre polynomials is given by

$$\int_{-1}^{1} \xi \, \psi_k \left(\xi\right) d\xi = \begin{cases} \frac{2}{3} & \text{if } k = 1 \\ 0 & \text{otherwise} \end{cases} \tag{A.20}$$

The 2^{nd} moment of the Legendre polynomials is given by

$$\int_{-1}^{1} \xi^2 \, \psi_k \left(\xi \right) d\xi = \begin{cases} \frac{2}{3} & \text{if } k = 0 \\ \frac{4}{15} & \text{if } k = 2 \\ 0 & \text{otherwise} \end{cases} \tag{A.21}$$

The above expressions for the 0^{th}, 1^{st} and 2^{nd} moments have been verified for polynomial orders $k = 0$ to 6.

Appendix B

Analyical Integrals involving the Maxwell-Boltzmann Distribution

The dimensionless form of the Maxwell-Boltzmann distribution is given by [1]

$$f^{MB}(\mathbf{c}) \equiv n^{MB}\left(\pi\, T^{MB}\right)^{-3/2} \exp\left(-\frac{\left\|\mathbf{c}-\mathbf{u}^{MB}\right\|^2}{T^{MB}}\right)$$

where n^{MB}, T^{MB} and $\mathbf{u}^{MB}$ are the dimensionless number density, temperature and mean velocity characterizing to the distribution f^{MB}.

B.1 Moments in Velocity Space

The moments of the Maxwell-Boltzmann distribution f^{MB} can be derived by making use of the following definite integrals [1].

$$I^0 \equiv \int_{-\infty}^{\infty} \exp\left(-\frac{c^2}{T}\right) dc = \sqrt{\pi\, T} \tag{B.1}$$

$$I^1 \equiv \int_{-\infty}^{\infty} c\left[\exp\left(-\frac{c^2}{T}\right)\right] dc = 0 \tag{B.2}$$

$$I^2 \equiv \int_{-\infty}^{\infty} c^2\left[\exp\left(-\frac{c^2}{T}\right)\right] dc = \sqrt{\pi\, T^3} \tag{B.3}$$

For simplicity in notation, let

$$H_k^0 \equiv \int_{-\infty}^{\infty} \exp\left(-\frac{\left[c_k - u_k^{MB}\right]^2}{T^{MB}}\right) dc_k \tag{B.4}$$

$$H_k^1 \equiv \int_{-\infty}^{\infty} c_k \left[\exp\left(-\frac{\left[c_k - u_k^{MB}\right]^2}{T^{MB}}\right)\right] dc_k \tag{B.5}$$

$$H_k^2 \equiv \int_{-\infty}^{\infty} c_k^2 \left[\exp\left(-\frac{\left[c_k - u_k^{MB}\right]^2}{T^{MB}}\right)\right] dc_k \tag{B.6}$$

$$\tag{B.7}$$

The 0^{th} moment of f^{MB} is given by

$$\begin{aligned} F^{0,MB} &= \int f^{MB} d^3\mathbf{c} \\ &= n^{MB} \left(\pi\, T^{MB}\right)^{-3/2} \prod_{k=1}^{3} H_k^0 \\ &= n^{MB} \end{aligned} \tag{B.8}$$

by making a substitution $c_k' = c_k - u_k^{MB}$ and applying the definite integral I^0 in equation B.1.

The 1^{st} moment of f^{MB} is given by

$$\begin{aligned} F_m^{1,MB} &= \int c_m f^{MB} d^3\mathbf{c} \\ &= n^{MB} \left(\pi\, T^{MB}\right)^{-3/2} H_m^1 \prod_{k=[1,3]\setminus\{m\}} H_k^0 \\ &= n^{MB}\, u_m^{MB} \end{aligned} \tag{B.9}$$

by making a substitution $c_k' = c_k - u_k^{MB}$, followed by applying the definite integrals I^1 and I^0 in equations B.2 and B.1 respectively.

The 2^{nd} principal moment of f^{MB} is given by

$$\begin{aligned} F_m^{2,MB} &= \int c_m^2 f^{MB} d^3\mathbf{c} \\ &= n^{MB} \left(\pi\, T^{MB}\right)^{-3/2} H_m^2 \prod_{k=[1,3]\setminus\{m\}} H_k^0 \\ &= n^{MB} \left(u_m^{MB\,2} + \frac{T^{MB}}{2} \right) \end{aligned} \tag{B.10}$$

by making a substitution $c_k' = c_k - u_k^{MB}$, followed by applying the definite integrals I^2, I^1 and I^0 in equations B.3, B.2 and B.1 respectively.

The 2^{nd} cross moment of f^{MB} is given by

$$\begin{aligned} F_{mj}^{\text{cross},MB} &= \int c_m\, c_j f^{MB} d^3\mathbf{c} \\ &= n^{MB} \left(\pi\, T^{MB}\right)^{-3/2} H_m^1\, H_j^1 \prod_{k=[1,3]\setminus\{m,j\}} H_k^0 \\ &= n^{MB}\, u_m^{MB}\, u_j^{MB} \end{aligned} \tag{B.11}$$

by making a substitution $c_k' = c_k - u_k^{MB}$, followed by applying the definite integrals I^1 and I^0 in equations B.2 and B.1 respectively.

B.2 Maxwell-Boltzmann Boundary Fluxes

The interested boundary fluxes in this thesis are essentially 1^{st} moments of a Maxwell-Boltzmann distribution over part of the velocity space. The Maxwell-Boltzmann distributions considered are the chosen equilibrium distribution f^{MB} and the wall distribution f^{wall}.

For simplicity in notation, let

$$P_k^{MB,1} \equiv \int_{u_k^{\rm w}}^{\infty} (c_k - u_k^{\rm w}) \exp\left(-\frac{\left[c_k - u_k^{MB}\right]^2}{T^{MB}}\right) dc_k \tag{B.12}$$

$$P_k^{\rm wall,1} \equiv \int_{u_k^{\rm w}}^{\infty} (c_k - u_k^{\rm w}) \exp\left(-\frac{\left[c_k - u_k^{\rm w}\right]^2}{T^{\rm wall}}\right) dc_k \tag{B.13}$$

$$L_k^{MB,1} \equiv \int_{-\infty}^{u_k^{\rm w}} (c_k - u_k^{\rm w}) \exp\left(-\frac{\left[c_k - u_k^{MB}\right]^2}{T^{MB}}\right) dc \tag{B.14}$$

$$L_k^{\rm wall,1} \equiv \int_{-\infty}^{u_k^{\rm w}} (c_k - u_k^{\rm w}) \exp\left(-\frac{\left[c_k - u_k^{\rm w}\right]^2}{T^{\rm wall}}\right) dc_k \tag{B.15}$$

$$H_k^{MB,0} \equiv \int_{-\infty}^{\infty} \exp\left(-\frac{\left[c_k - u_k^{MB}\right]^2}{T^{MB}}\right) dc \tag{B.16}$$

$$H_k^{\rm wall,0} \equiv \int_{-\infty}^{\infty} \exp\left(-\frac{\left[c_k - u_k^{\rm w}\right]^2}{T^{\rm wall}}\right) dc \tag{B.17}$$

where c_k and u_k^w are, respectively, the normal component of the gas molecule velocity and wall velocity to the wall $x_k = x_{k,max}$ or $x_k = x_{k,min}$ ($k = 1, 2$ or 3). The dimensionless temperature of the wall is denoted by $T^{\rm wall}$.

The boundary fluxes to be evaluated at the wall $x_m = x_{m,max}$ are

$$\begin{aligned} F^{MB} &= \int_{c_m > u_m^w} (c_m - u_m^w)\, f^{MB} d^3\mathbf{c} \\ &= n^{MB} \left(\pi\, T^{MB}\right)^{-3/2} P_m^{MB,1} \prod_{k=[1,3]\setminus\{m\}} H_k^{MB,0} \end{aligned} \tag{B.18}$$

and

$$\begin{aligned} F^{\rm wall} &= \int_{c_m < u_m^w} (c_m - u_m^w) \left(f^{\rm wall}\right) d^3\mathbf{c} \\ &= \left(\pi\, T^{\rm wall}\right)^{-3/2} L_m^{\rm wall,1} \prod_{k=[1,3]\setminus\{m\}} H_k^{\rm wall,0} \end{aligned} \tag{B.19}$$

while that to be evaluated at the wall $x_m = x_{m,min}$ are

$$\begin{aligned} F^{MB} &= \int_{c_m < u_m^w} (c_m - u_m^w)\, f^{MB} d^3\mathbf{c} \\ &= n^{MB} \left(\pi\, T^{MB}\right)^{-3/2} L_m^{MB,1} \prod_{k=[1,3]\setminus\{m\}} H_k^{MB,0} \end{aligned} \tag{B.20}$$

and

$$\begin{aligned} F^{\text{wall}} &= \int_{c_m > u_m^w} (c_m - u_m^w) \left(f^{\text{wall}}\right) d^3\mathbf{c} \\ &= \left(\pi\, T^{\text{wall}}\right)^{-3/2} P_m^{\text{wall},1} \prod_{k=[1,3]\setminus\{m\}} H_k^{\text{wall},0} \end{aligned} \tag{B.21}$$

By making a substitution $c_k' = c_k - u_k^{MB}$ and applying the definite integral I^0 in equation B.1,

$$H_k^{MB,0} = \sqrt{\pi\, T^{MB}} \tag{B.22}$$

$$H_k^{\text{wall},0} = \sqrt{\pi\, T^{\text{wall}}} \tag{B.23}$$

for all $k = [1, 3]$. Similarly, by making a substitution $c_m' = c_m - u_m^w$ and applying standard integration techniques,

$$P_m^{\text{wall},1} = \frac{T^{\text{wall}}}{2} \tag{B.24}$$

$$L_m^{\text{wall},1} = -\frac{T^{\text{wall}}}{2} \tag{B.25}$$

for all $m = [1, 3]$.

To evaluate $P_m^{MB,1}$ at the wall $x_m = x_{m,max}$, a substitution $c_m' = c_m - u_m^{MB}$ is used together with standard integration techniques to obtain

$$\begin{aligned} P_m^{MB,1} &= \int_{u_{rel}}^{\infty} (c_m' - u_{rel}) \exp\left(-\frac{{c_m'}^2}{T^{MB}}\right) dc_m' \\ &= \frac{T^{MB}}{2} \exp\left(-\frac{u_{rel}^2}{T^{MB}}\right) - u_{rel} E^{\text{right}}(u_{rel}) \end{aligned} \tag{B.26}$$

where $u_{rel} = u_m^w - u_m^{MB}$ and the function $E^{\text{right}}(u_{rel})$ is given by

$$\begin{aligned} E^{\text{right}}(u_{rel}) &= \int_{u_{rel}}^{\infty} \exp\left(-\frac{{c'_m}^2}{T^{MB}}\right) dc'_m \\ &= \int_0^{\infty} \exp\left(-\frac{{c'_m}^2}{T^{MB}}\right) dc'_m \pm \int_0^{u_{rel}} \exp\left(-\frac{{c'_m}^2}{T^{MB}}\right) dc'_m \\ &= \frac{\sqrt{\pi\, T^{MB}}}{2} \pm \sqrt{T^{MB}} \int_0^{\frac{u_{rel}}{\sqrt{T^{MB}}}} \exp\left(-\left(\frac{c'_m}{\sqrt{T^{MB}}}\right)^2\right) d\left(\frac{c'_m}{\sqrt{T^{MB}}}\right) \\ &= \frac{\sqrt{\pi\, T^{MB}}}{2}\left(1 \pm \text{erf}\left(\frac{u_{rel}}{\sqrt{T^{MB}}}\right)\right) \end{aligned} \tag{B.27}$$

Similarly, $L_m^{MB,1}$ can be evaluated at the wall $x_m = x_{m,min}$ as

$$\begin{aligned} L_m^{MB,1} &= \int_{-\infty}^{u_{rel}} (c'_m - u_{rel}) \exp\left(-\frac{{c'_m}^2}{T^{MB}}\right) dc'_m \\ &= -\frac{T^{MB}}{2} \exp\left(-\frac{{u_{rel}}^2}{T^{MB}}\right) - u_{rel} E^{\text{left}}(u_{rel}) \end{aligned} \tag{B.28}$$

where

$$\begin{aligned} E^{\text{left}}(u_{rel}) &= \int_{-\infty}^{u_{rel}} \exp\left(-\frac{{c'_m}^2}{T^{MB}}\right) dc'_m \\ &= \int_{-\infty}^{0} \exp\left(-\frac{{c'_m}^2}{T^{MB}}\right) dc'_m \pm \int_0^{u_{rel}} \exp\left(-\frac{{c'_m}^2}{T^{MB}}\right) dc'_m \\ &= \frac{\sqrt{\pi\, T^{MB}}}{2}\left(1 \pm \text{erf}\left(\frac{u_{rel}}{\sqrt{T^{MB}}}\right)\right) \end{aligned} \tag{B.29}$$

The + sign corresponds to walls moving towards each other ($u_{rel} < 0$ for the wall $x_m = x_{m,max}$ and $u_{rel} > 0$ for the wall $x_m = x_{m,min}$) while the − sign corresponds to walls moving apart ($u_{rel} > 0$ for the wall $x_m = x_{m,max}$ and $u_{rel} < 0$ for the wall $x_m = x_{m,min}$). The last step in the derivation of $E^{\text{right}}(u_{rel})$ and $E^{\text{left}}(u_{rel})$ make use of the error function definition

$$\text{erf}\,(b) = \frac{2}{\sqrt{\pi}} \int_0^b \exp\left(-y^2\right) dy \tag{B.30}$$

Using the above results, the boundary fluxes at the wall are given by

$$F^{MB} = n^{MB}\left[\mp\frac{1}{2}\sqrt{\frac{T^{MB}}{\pi}}\exp\left(-\frac{u_{rel}^2}{T^{MB}}\right) - \frac{u_{rel}}{2}\left(1+\mathrm{sgn}(\mathbf{u}^{\mathrm{wall}}\cdot\tilde{n})\,\mathrm{erf}\left(\frac{u_{rel}}{\sqrt{T^{MB}}}\right)\right)\right] \tag{B.31}$$

and

$$F^{\mathrm{wall}} = \pm\frac{1}{2}\sqrt{\frac{T^{\mathrm{wall}}}{\pi}} \tag{B.32}$$

The symbol $\tilde{n}$ denotes the unit normal to the wall pointing into the gas and $\mathbf{u}^{\mathrm{wall}}$ represents the wall velocity. Hence, the expression "$\mathrm{sgn}(\mathbf{u}^{\mathrm{wall}}\cdot\tilde{n})$" takes on a value of $+1$ or -1 when the walls are moving towards or apart from each other respectively. The signs $\mp$ in F_{MB}, as well as $\pm$ in F^{wall}, correspond, respectively, to boundary fluxes evaluated at the walls $x_m = x_{m,min}$ or $x_m = x_{m,max}$ ($m = 1, 2$ or 3).

Bibliography

[1] W. G. Vincenti and C. H. Kruger. *Introduction to Physical Gas Dynamic.* Krieger, Florida, 1965.

[2] G. A. Bird. *Molecular Gas Dynamics and the Direct Simulation of Gas Flows.* Clarendon Press, Oxford, 1994

[3] F. J. Alexander and A. L. Garcia. "The direct simulation Monte Carlo method". *Computers in Physics,* **11** *(6)*, pp. 588–593, 1997

[4] N. G. Hadjiconstantinou, A. L. Garcia, M. Z. Bazant and G. He. "Statistical error in particle simulations of hydrodynamic phenomena". *Journal of Computational Physics,* **187**, pp. 274–297, 2003.

[5] L. L. Baker and N. G. Hadjiconstantinou. "Variance reduction for Monte Carlo solutions of the Boltzmann equation". *Physics of Fluids,* **17**, art. no. 051703, 2005

[6] B. Cockburn and C. Shu. "Runge-Kutta Discontinuous Galerkin Methods for convection-dominated problems". *Journal of Scientific Computing,* **16**, 173, 2001.

[7] G. E. Karniadakis and S. J. Sherwin. *Spectral/hp element methods for CFD.* Oxford University Press, 1999.

[8] S. Gottlieb, C.-W. Shu and E. Tadmor. "Strong stability-preserving high-order time discretization methods". *SIAM Review,* **43** *(1)*, pp. 89–112, 2001.

[9] L. L. Baker. "Efficient numerical methods for solving the Boltzmann equation for small scale flows". Ph.D. thesis, Massachusetts Institute of Technology, June 2007.

[10] L. L. Baker. "Efficient numerical methods for solving the Boltzmann equation for small scale flows". Master's thesis, Massachusetts Institute of Technology, February 2004.

[11] C. Cercignani. *The Boltzmann Equation and its Applications*. Springer-Verlag, New York, 1988.

[12] F. Reif. *Fundamentals of Statistical and Thermal Physics*. McGrawHill, Boston, 1965.

[13] C. Cercignani and A. Daneri. "Flow of a rarefied gas between two parallel plates". *Journal of Applied Physics,* **34** *(12)*, 1963.

[14] Y. Sone and M. Hasegawa. "Poiseuille and Thermal Transpiration Flows of a Rarefied Gas through a Rectangular Pipe". *Shinku (Journal of the Vacuum Society of Japan,* **30** *(5)*, 1987.

[15] Y. Sone. *Kinetic Theory and Fluid Dynamics*. Birkhauser, 2002.

[16] N. G. Hadjiconstantinou. "The limits of Navier-Stokes theory and kinetic extensions for describing small scale gaseous hydrodynamics". *Physics of Fluids,* **18** *(111301)*, 2006.

[17] G. Arfken. "Ch. 12 Legendre Functions". *Mathematical Methods for Physicists*. 3rd ed., FL: Academic Press, Orlando, pp. 700, 1985.

[18] H. M. Lui. "Runge-Kutta Discontinuous Galerkin Method for the Boltzmann Equation". Master's thesis, Massachusetts Institute of Technology, September 2006.

[19] P. LeSaint and P. A. Raviart. "On a finite element method for solving the neutron transport equation". *Mathematical Aspects of Finite Elements in Partial*

Differential Equations. C. de Boor, ed., Academic Press, New York, pp. 89-123, 1974.

[20] T. Ohwada, Y. Sone and K. Aoki. "Numerical analysis of the Poiseuille and thermal transpiration flows between two parallel plates on the basis of the Boltzmann equation for hard sphere molecules". *Physics of Fluids,* **1** (12), 1989

[21] K. Aoki. "Dynamics of Rarefied Gas Flows: Asymptotic and Numerical Analyses of the Boltzmann Equation". *AIAA paper* 2001-0874.